Key Points:
- We have calculated each term of the surface energy budget during the first 2500 sols of the Mars Science Laboratory mission
- We have analyzed the variation of each term from diurnal to interannual timescales in relation to the mechanisms causing the variations
- Our results are important in preparation for the human exploration of Mars to evaluate the consistency with predictions from models

Correspondence to:
G. M. Martínez,
gmartinez@lpi.usra.edu

Author Contributions:
Conceptualization: G. M. Martínez, N. O. Rennó, H. Savijärvi, M. Torre, T. H. McConnochie, A. Sánchez-Lavega
Data curation: G. M. Martínez, M. T. Lemmon, E. Sebastián
Formal analysis: G. M. Martínez, E. Fischer
Funding acquisition: G. M. Martínez, N. O. Rennó
Investigation: G. M. Martínez, S. D. Guzewich
Methodology: G. M. Martínez, A. Vicente-Retortillo, A. R. Vasavada, C. E. Newman, H. Savijärvi

The Surface Energy Budget at Gale Crater During the First 2500 Sols of the Mars Science Laboratory Mission

G. M. Martínez[1,2] ⓘ, A. Vicente-Retortillo[2,3], A. R. Vasavada[4] ⓘ, C. E. Newman[5] ⓘ, E. Fischer[2] ⓘ, N. O. Rennó[2], H. Savijärvi[6,7], M. de la Torre[4] ⓘ, I. Ordóñez-Etxeberria[8,9], M. T. Lemmon[10] ⓘ, S. D. Guzewich[11] ⓘ, T. H. McConnochie[12], E. Sebastián[3], R. Hueso[8] ⓘ, and A. Sánchez-Lavega[8] ⓘ

[1]Lunar and Planetary Institute, Universities Space Research Association, Houston, TX, USA, [2]Department of Climate and Space Sciences and Engineering, University of Michigan, Ann Arbor, MI, USA, [3]Centro de Astrobiología (INTA-CSIC), Madrid, Spain, [4]Jet Propulsion Laboratory, California Institute of Technology, Pasadena, CA, USA, [5]Aeolis Research, Chandler, AZ, USA, [6]Institute for Atmospheric and Earth System Research / Physics, University of Helsinki, Helsinki, Finland, [7]Finnish Meteorological Institute, Helsinki, Finland, [8]Universidad del País Vasco, Bilbao, Spain, [9]Planetario de Pamplona, Pamplona, Spain, [10]Space Science Institute, College Station, TX, USA, [11]NASA Goddard Spaceflight Center, Greenbelt, MD, USA, [12]Department of Astronomy, University of Maryland, College Park, MD, USA

Abstract We use in situ environmental measurements by the Mars Science Laboratory (MSL) mission to obtain the surface energy budget (SEB) across Curiosity's traverse during the first 2500 sols of the mission. This includes values of the downwelling shortwave solar radiation, the upwelling solar radiation reflected by the surface, the downwelling longwave radiation from the atmosphere, the upwelling longwave radiation emitted by the surface, the sensible heat flux associated with turbulent motions, and the latent heat flux associated with water phase changes. We then analyze their temporal variation on different timescales and relate this to the mechanisms causing these variations. Through its Rover Environmental Monitoring Station, MSL allows for a more accurate determination of the SEB than its predecessors on Mars. Moreover, the unprecedented duration, cadence, and frequency of MSL environmental observations allow for analyses of the SEB from diurnal to interannual timescales. The results presented in this article can be used to evaluate the consistency with predictions from atmospheric numerical models, to validate aerosol radiative properties under a range of dust conditions, to understand the energy available for solar-powered missions, and to enable comparisons with measurements of the SEB by the Perseverance rover at Jezero crater.

Plain Language Summary The primary energy input at the Martian surface is the solar radiation, which depends on the time of the day and season, geographical location (latitude and altitude), and atmospheric dust and gas abundances. Another energy input is the thermal atmospheric forcing, which depends on the vertical distribution of dust and water ice aerosols as well as CO_2 and H_2O molecules. Together with the reflected solar radiation and the thermal radiation emitted by the surface, these four terms make up the net radiative forcing of the surface. In response to it, energy outputs as turbulent motions and water phase changes emerge to cool down/warm up the ground. The remaining energy is available to control the thermal environment in the surface and shallow subsurface through conduction into the soil. By using first-of-their-kind measurements from the Mars Science Laboratory mission, we calculate the energy inputs and outputs across Curiosity's traverse over the first 2500 Martian days of the mission. We then analyze their temporal variations and relate this to the mechanisms causing such variations. An accurate determination of the surface energy budget is key to preparing for the human exploration of Mars because it contributes to improvements in the predictive capabilities of numerical models.

1. Introduction

Conservation of energy at the surface–atmosphere interface of a planetary object requires that

$$G = \left(SW \downarrow - SW \uparrow \right) + \left(LW \downarrow - LW \uparrow \right) - TF - LF, \tag{1}$$

Journal of Geophysical Research: Planets

Project Administration: G. M. Martínez
Resources: G. M. Martínez
Software: G. M. Martínez
Supervision: G. M. Martínez
Validation: G. M. Martínez
Visualization: G. M. Martínez
Writing – original draft: G. M. Martínez, A. Vicente-Retortillo, A. R. Vasavada, C. E. Newman, R. Hueso
Writing – review & editing: G. M. Martínez, A. Vicente-Retortillo, A. R. Vasavada, E. Fischer, N. O. Rennó, H. Savijärvi, S. D. Guzewich, R. Hueso, A. Sánchez-Lavega

where G represents the net heat flux into the soil, SW↓ is the downwelling shortwave solar radiation flux transmitted through the air, SW↑ is the upwelling solar radiation flux reflected by the surface, LW↓ is the downwelling longwave radiation flux from the whole atmosphere, LW↑ is the upwelling longwave radiation flux emitted by the surface, TF is the sensible heat flux associated with turbulent motions, and LF is the latent heat flux associated with phase changes (Figure 1). Equation 1 is known as the surface energy balance (SEB).

Variations in the Martian SEB are fundamental in driving the atmospheric energy balance and powering the global atmospheric circulation (e.g., Tabataba-Vakili et al., 2015). The primary surface forcing on Mars is SW↓, which depends on the time of day, distance from the Sun, season (as a function of solar longitude, Ls), geographical location (through latitude and elevation), atmospheric abundances of gas molecules (e.g., CO_2 and H_2O), and abundances and optical properties of aerosols (e.g., dust, water ice, and CO_2 ice) (Haberle et al., 1993; Savijärvi et al., 2005; Vicente-Retortillo et al., 2015). Another surface forcing is LW↓, which depends on the vertical distribution of "greenhouse" airborne aerosols (dust and water ice) and molecular species (CO_2 and H_2O; Smith et al., 1996; Määttänen & Savijärvi, 2004). Together with SW↑, which depends on the surface albedo (Fenton et al., 2007), and LW↑, which depends on the temperature and thermal infrared emissivity of the ground (Smith et al., 2000), these four terms comprise the net radiative forcing of the surface. In response to it, TF and LF usually emerge to remove heat from the soil to the air during the daytime through upward heat transfer and sublimation and to warm the soil at night through downward heat transfer and deposition, respectively. Although the sensible and latent heat flux terms cannot efficiently cool down/warm up the soil on Mars due to the extremely low atmospheric density (100 times lower than on Earth) and absolute water content (~1000 times lower than on Earth; Martínez et al., 2017), TF is thought to play an important role in the development of convective vortices that propagate upward in the atmosphere and efficiently mix aerosols (Rafkin et al., 2001; Renno et al., 1998; Spiga et al., 2010). The difference between the net radiative forcing and the response terms constitutes the energy available for conduction into the soil (G), which controls diurnal variations in the surface and shallow subsurface temperatures (e.g., Martínez et al., 2014).

Due to the lack of direct ground-based measurements, each term of the SEB in Equation 1 has typically been simulated in the past work by matching a model's output to the measured values of air temperature, horizontal wind speed, and surface pressure. Following this procedure, the SEB has been estimated at the two Viking Lander (Haberle et al., 1993; Savijärvi, 1995; Savijärvi et al., 2018; Sutton et al., 1978), Mars Pathfinder (Savijärvi, 1999), and Phoenix (Savijärvi and Määttänen, 2010) landing sites. Similarly, the SEB at the two Mars Exploration Rover (MER) landing sites has been simulated by matching a model's output to the vertical temperature profile retrieved from the mini-TES instrument (Savijärvi, 2012). At each landing site, simulated values of the SEB are subjected to uncertainties in the model parameters, such as optical properties and vertical distribution of dust and water ice aerosols (which affect SW↓ and LW↓) and ground temperature and geophysical properties of the terrain (which affect SW↑, LW↑, and G).

Through its Rover Environmental Monitoring Station (REMS) instrument suite, the Mars Science Laboratory (MSL) mission allows for a more accurate determination of the SEB than its predecessors. Moreover, the unprecedented duration, data measuring, and storage capabilities of MSL allow analyses of the SEB from interannual to diurnal timescales. REMS is a suite of meteorological sensors measuring UV radiation fluxes, ground and air temperature, relative humidity, pressure, and horizontal wind speed and direction (Gómez-Elvira et al., 2012). The REMS UV sensor (UVS) is the first to measure the UV radiation flux at the surface of Mars (Smith et al., 2016; Vicente-Retortillo et al., 2020). Similarly, the REMS ground temperature sensor (GTS) has been measuring full diurnal cycles for the first time on Mars, as the previous ground temperature measurements by the MER and Phoenix (PHX) missions were limited to certain periods of the day and season (Smith et al., 2006; Spanovich et al., 2006; Zent et al., 2010). Synergistically with REMS, the Mastcam instrument has been measuring atmospheric dust opacities at the wavelengths of 440 and 880 nm (Smith et al., 2016).

In this article, we use in situ measurements from the REMS and Mastcam instruments to obtain the SEB across Curiosity's traverse through sol 2500 of the MSL mission. We then analyze the variation of each term of the SEB from diurnal to interannual timescales. The results presented in this article can be used to evaluate the consistency with predictions from atmospheric numerical models, as their near-surface
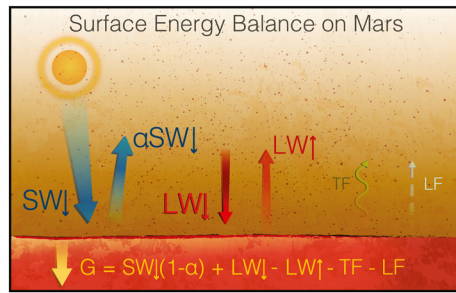
Figure 1. Schematic of the surface energy balance on Mars. By convention, radiative fluxes directed toward the surface (warming) and nonradiative fluxes (TF, LF, and G) directed away from the surface (cooling) are taken positive (Garrat, 1992). Note that radiative fluxes are plugged into Equation 1 as positive values, whereas nonradiative fluxes can be plugged in as positive or negative depending on whether they are directed away from or toward the surface. The reflected solar radiation can be expressed as SW↑ = αSW↓, where α represents the Lambertian surface albedo. The arrows are not to scale. Image Credit: Etor Eceiza & Germán Martínez.

environmental outputs (e.g., temperature and radiation fluxes) strongly depend on the simulated SEB values (Greybush et al., 2019; Newman et al., 2019; Pla-Garcia et al., 2016; Savijärvi et al., 2020; Spiga et al., 2020). In combination with numerical models, the determination of the downwelling SW and LW radiative fluxes provides an excellent opportunity to determine aerosol abundances and their variations (Smith et al., 2016; Vicente-Retortillo et al., 2021) to validate aerosol radiative properties for a range of dust conditions, including global dust storms (Savijärvi et al., 2020), and to indirectly detect the presence of water ice clouds at nighttime (de la Torre-Juarez et al., 2019; Vasavada et al., 2017). Furthermore, the determination of the downwelling SW radiative and turbulent heat fluxes is important to understand the energy available for solar-powered missions and to infer the periodic removal of dust from solar panels caused by convective phenomena such as dust devils (Lorenz et al., 2020; Vicente-Retortillo et al., 2018). Finally, the results of this study will enable comparisons with measurements of the SEB by the Perseverance rover at Jezero crater (Farley et al., 2020; Rodriguez-Manfredi et al., 2020).

Ground-based observations and modeled quantities used in this study are described in Section 2. The methodology used to obtain each term of the SEB described by Equation 1 is explained in Section 3. The results are presented in Section 4, where the variation of the SEB from diurnal to interannual timescales is analyzed in relation to the mechanisms causing such variations. Discussion of the results and future work are presented in Section 5, while the summary and conclusions are presented in Section 6.

2. Data

In this article, we use surface-based measurements by the REMS and Mastcam instruments (Section 2.1), modeled values of horizontal wind speed (Section 2.2), and model-derived values of thermal inertia and albedo (Section 2.3) based on REMS and Mastcam data through sol 2500 of the MSL mission.

2.1. REMS and Mastcam Observations

The REMS instrument is composed of six sensors measuring UV radiation fluxes, ground and air temperature, relative humidity, pressure, and horizontal wind speed and direction (Gómez-Elvira et al., 2012). The wind sensor was damaged at landing, which resulted in systematic observational biases when the wind was coming from certain directions. As a result, the temporal coverage of reliable wind measurements was significantly reduced (Newman et al., 2017). Around sol 1500, the wind sensor stopped working entirely.

REMS uses a nominal measuring strategy consisting of 5-min-long periods at the beginning of each hour during which each quantity is sampled at 1 Hz (Gómez-Elvira et al., 2014). In addition, full hour sample periods, also at 1 Hz, are interspersed to cover every hour of the sol at least once per six-sol period (Newman et al., 2017). Mastcam directly images the Sun, from which aerosol optical depth (τ) at the wavelengths of 440 and 880 nm is derived. These images are typically taken every three to seven sols in the vicinity of noon (Lemmon et al., 2019).

Here, we use REMS measurements performed nominally at the beginning of each hour to produce complete coverages of the diurnal cycle through the mission. By averaging REMS measurements of the highest confidence possible over the first five minutes of each hour, we obtain "hourly" values of pressure (P), air temperature (T_a), ground temperature (T_g), relative humidity (RH), and UV flux in the 200–380 nm spectral band. We also obtain hourly values of air density as $\rho_a = P/(R \times T_a)$, where $R = 191$ J kg^{-1} K^{-1} is the gas constant of the Martian atmosphere. For each of these quantities, we only consider sols on which full diurnal coverage is attained. While averages of P and T_a (and thus ρ) are straightforwardly obtained using measurements available in the NASA Planetary Data System (PDS), a sensor-specific approach described below is taken to produce hourly values of T_g, RH, and UV.

Ground temperature measurements performed during the first couple of minutes of each hour, just after the GTS is turned on, are subjected to strong electronic noise and bias error during thermal stabilization of amplification electronics. This effect is most noticeable in winter at night, when temperatures are the lowest. To avoid this effect, we average GTS measurements taken during the last two minutes of each 5-min-long measuring period, when temperatures are stable.

Similarly, RH measurements are affected by the heating effect of the sensor, resulting in significant under-estimations of the actual atmospheric RH. To avoid this effect, we only consider RH measurements taken during the first four seconds of each hour, which virtually show the same value (see Section 3.6 of Martínez et al., 2017, for further details). As an RH-derived product, we calculate the water vapor volume mixing ratio as $VMR = RH \times e_s(T)/P$, where e_s is the saturation vapor pressure over ice (Savijärvi and Määttänen, 2010). Due to the extremely low RH during the daytime (<5% between 10:00 and 18:00 Local Mean Solar Time (LMST) throughout the year) and the correspondingly high relative error, REMS-derived VMR values can only be obtained reliably during nighttime (Savijärvi et al., 2016). In particular, VMR values are most accurate between 04:00 and 06:00 LMST, when diurnal RH values are largest (Martínez et al., 2016).

Finally, the REMS UV sensor has been exposed to dust deposition due to its location on Curiosity's deck. In addition, inaccuracies in the original angular response calibration functions led to large discrepancies between measured and physically expected UV fluxes when the solar zenith angle is between 20° and 55°. We have corrected UV fluxes for both effects (Vicente-Retortillo et al., 2020) and have made this new data set available in the NASA PDS (https://atmos.nmsu.edu/PDS/data/mslrem_1001/DATA_UV_CORRECTED/). Using this corrected data set, we have obtained hourly values of UV fluxes in the 200–380 nm band using the measurements performed during nominal operations.

By processing REMS measurements as explained above, and to help interpret results of the SEB shown in Section 4, we show in Figure 2 interannual and seasonal variations of the environmental conditions at Gale during the first 2500 sols of the MSL mission. The most striking aspects of Figure 2 are (a) the larger inter-annual variability of opacity, UV flux, and temperature during the perihelion (Ls = 180°–360°) compared to the aphelion season (Ls = 0°–180°); (b) the 2018/MY34 global dust storm (purple squares at Ls ∼ 195°) (Guzewich et al., 2019; Sánchez-Lavega et al., 2019); (c) the year-to-year decrease in surface pressure and air density at the same Ls as the Curiosity rover traversed toward higher elevations (Figures 2c and 2d); (d) the increase in water vapor VMR from about sol 1800 onward (MY 34, Ls ∼ 54°; Figure 2h), when the Curiosity rover started to climb Aeolis Mons (Savijärvi et al., 2019); and (e) the saturated conditions reached in the near-surface air in MY 35 at Ls ∼ 90°, which might have resulted in the formation of surface frost (Gough et al., 2020).

2.2. Modeled Wind Speeds

Unfortunately, REMS wind speed data contain many uncertainties, data gaps, and biases (Gomez-Elvira et al., 2014; Newman et al., 2017; Viúdez-Moreiras et al., 2019a, 2019b). These are a result of: (a) the failure of most wind sensor components on the rear-/side-pointing wind sensor on landing, which left only the forward-pointing wind sensor working and prevented accurate measurements of wind blowing from the hemisphere to the rear of the rover; (b) large electronic noise in data from the remaining sensor during the coldest 7–10 h of each sol, depending on season; and (c) the complete failure of the remaining wind sensor on sol ∼1500 of the mission.

We therefore use the MarsWRF atmospheric model, running as a global model with higher-resolution nests centered over and fully covering MSL's traverse, to predict wind speed as a function of time of sol, location, and season. These results are taken from the model version and setup described in Newman et al. (2017). We use the results from the innermost nest (run at ∼1.4-km horizontal grid spacing) of the "vertical grid B" simulation, as the latter was found to more realistically reproduce wind data taken during a campaign in which the rover faced multiple directions over several sols to obtain the most complete wind measurements of the MSL mission. When used to predict sand transport and "dust devil activity" (Rennó et al., 1998), respectively, these wind predictions also resulted in a far better match to the observed orientation and motion of the Bagnold Dunes (Newman et al., 2017) and a better match to the observed spatiotemporal variation in vortex activity (Newman et al., 2019) than the predictions using "vertical grid A."
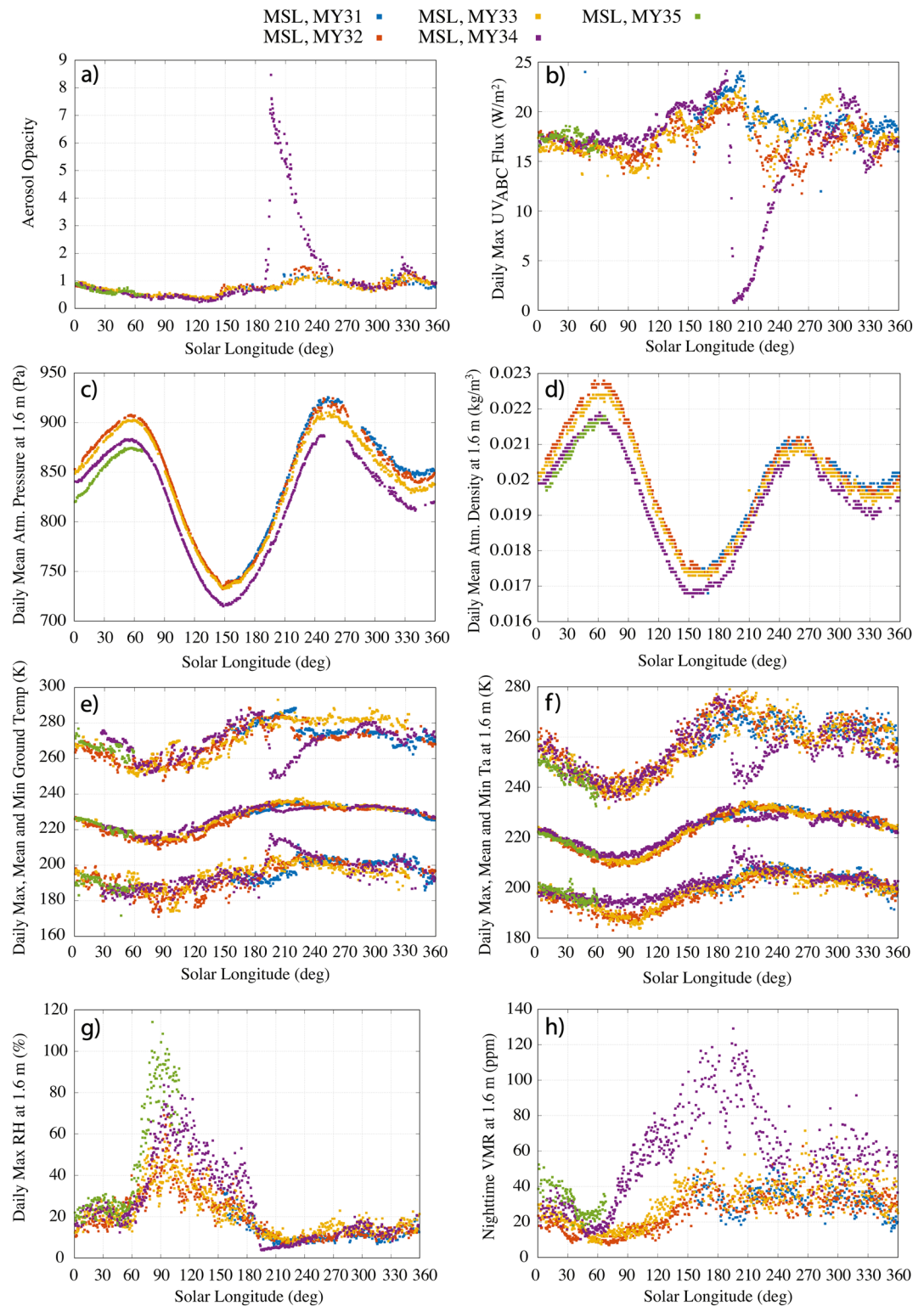
Figure 2. Environmental conditions along Curiosity's traverse: Interannual and seasonal evolution of (a) the aerosol opacity; (b) daily maximum UV$_{ABC}$ (200–380 nm) flux; (c and d) daily mean atmospheric pressure and air density; (e and f) daily maximum, mean, and minimum ground and air temperature; (g) daily maximum atmospheric relative humidity; and (h) nighttime water vapor volume mixing ratio during the first 2500 sols of the Mars Science Laboratory mission. Color code is used to represent different Martian Years.

Figure 3. Daily maximum horizontal wind speed at 1.5 m simulated by the MarsWRF General Circulation Model. Details of the simulations are given in Newman et al. (2017, 2019).

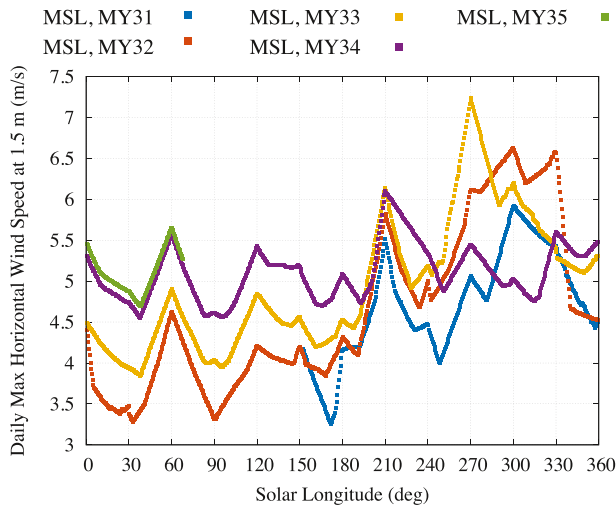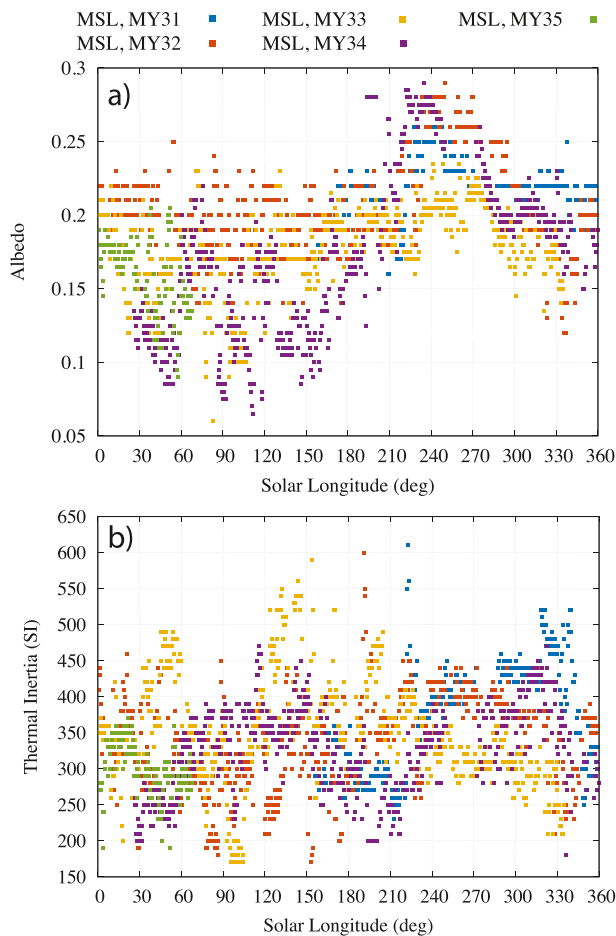**Figure 4.** Albedo (a) and thermal inertia (b) along Curiosity's traverse through sol 2500 obtained following the methodology described in Vasavada et al. (2017).

Because small horizontal grid spacings are required to resolve the topography of Gale crater, it was not possible to run the nested model for a complete Mars year. Instead, the nested model was run for 7 sols every 30° of Ls, outputting 1.5-m altitude winds every 10 Mars minutes. The lowest model layer is centered at ~145 m in this simulation; hence, winds in this layer are extrapolated to 1.5 m within MarsWRF's boundary layer scheme (Hong & Pan, 1996), using the log-wind profile modified for the applicability to stable, neutral, and unstable conditions (e.g., Stensrud, 2009; Stull, 2012). The 1.5-m winds were averaged over each set of 7 sols for each time of sol and location, providing a predicted wind for each 30°Ls band, time of sol, and location. These winds were then interpolated to the rover's position along its traverse in each mission sol and interpolated in Ls to find the prediction for that sol, resulting in wind speeds simulated every 10 min.

Figure 3 shows the daily maximum of the interpolated, 7-sol averaged wind speed at the rover's location over nearly four Mars years, as predicted using this method. Note too that this MarsWRF simulation prescribed the atmospheric dust distribution to be typical of a Mars year without major dust storms; thus, the results shown here are not representative of a particular MSL mission year or sol, other than representing year-to-year changes due to the changing rover position along its traverse. Because MarsWRF is a mesoscale model, flows are controlled by how the topography and other surface properties vary at the model's resolution (~1.4 km). Outside of major dust storms, year-to-year changes in the dust distribution at a given Ls are relatively small (MY34, Figure 2a) and thus, should have a relatively small impact on simulated winds. Additionally, we note that MarsWRF uses thermal inertia and albedo values derived from the satellite at much larger spatial scales than those obtained here (which correspond to the field of view of REMS/GTS; Section 2.3). Although the differences between simulated and observed T_g and T_a are significant due to the spatial scale, the effects on winds are smaller (see Figure 7 in Newman et al., 2019). The reader is referred to Newman et al. (2019) for interpretations of winds variations at different timescales across Curiosity's traverse.

2.3. Model-derived Albedo and Thermal Inertia

Figure 4 shows the values of albedo and thermal inertia that we assign to each point along Curiosity's traverse. These values were derived using the methods and model described in Vasavada et al. (2017). REMS measurements of ground temperature over each diurnal cycle are compared with predictions from a 1-D surface-atmosphere thermal model (THM) in order to simultaneously solve for the best-fit thermally derived albedo and apparent thermal inertia. Despite THM not being able to accurately simulate T_g during sunrise and sunset on most sols, the method followed in Vasavada et al. (2017) to calculate both quantities is barely sensitive to this mismatch. In particular, thermal inertia was derived by minimizing the square of the difference between the measured and modeled diurnal amplitude of T_g. Since the diurnal maximum and minimum ground temperature typically occurs at times (~13 and ~6 LMST, respectively), when THM accurately matches the observations, the diurnal amplitude of T_g is accurately simulated by this model (see Vasavada et al., 2017 and Figure 14a in the main text). Similarly, albedo was derived by minimizing the square of the difference between the measured and modeled time

average of T_g^4 (i.e., proportional to the total absorbed/emitted energy over the sol). Despite the different shapes during sunrise and sunset between THC-derived (or SCM-derived) and REMS-observed T_g curves, the integrated energy of both curves compares well (Vasavada et al., (2017)).

The model is run using Mastcam values of atmospheric dust opacity and a parameterized radiative contribution from water ice clouds/hazes. The estimated uncertainty in thermal inertia and albedo is ±50 SI and ±0.025, respectively. The ~100-m² footprint of the REMS ground temperature sensor typically contains a mix of surface materials, but the derived values clearly distinguish between surfaces observed to be dominated by loose materials, mudstone, and sandstone. For the present work, the derivations through sol 1337 of Curiosity's mission in Vasavada et al. (2017) were extended to cover sols from 1338 to 2500.

While thermal inertia variations do not follow any temporal pattern, the albedo values peak between Ls ∼ 210° and Ls ∼ 270° every MY. This suggests that bright dust is deposited on the regolith at Gale during southern summer. A further understanding of this phenomenon would require additional modeling efforts in combination with the analyses of ground-based and orbital observations and thus is left for future work as discussed in Section 5.

3. Methodology

3.1. Shortwave Fluxes

To calculate hourly values of the downwelling shortwave solar radiation, SW↓, we used corrected UV fluxes in the 200–380 nm band (UV_{ABC}), dust aerosol opacity at the wavelength of 880 nm, and the COMIMART radiative transfer model (Vicente-Retortillo et al., 2015, 2020).

Depending on the solar zenith angle (θ) relative to the rover frame (zenith at $\theta = 0°$), we follow different approaches for the calculation of SW↓. When $\theta < 55°$ (corresponding to about 60% of UV measurements performed with the Sun above the horizon, and covering the 8–15 LMST period at $L_s \sim 100°$–250° and the 9–16 LMST period during the rest of the year), we converted hourly values of corrected UV fluxes in the 200–380 nm to broadband (200–3000 nm) shortwave fluxes using the radiative transfer model COMIMART (Vicente-Retortillo et al., 2015). Dust radiative properties involved in the calculations were derived from CRISM (Wolff et al., 2009), MARCI (Wolff et al., 2010), Mastcam, and REMS (Savijärvi et al., 2020) observations. These properties depend on wavelength (Wolff et al., 2009), with the single scattering albedo in the UV range being smaller than the mean value in the entire shortwave range. Therefore, the ratio between UV and SW values depends on atmospheric opacity and solar zenith angle (e.g., Vicente-Retortillo et al., 2015, for a comparison between UV and near-infrared fluxes). For this reason, the conversion factor was calculated as a function of the atmospheric opacity and the solar zenith angle, improving in this way the accuracy of the broadband shortwave values.

In the calculation of the conversion factors, we assume that dust radiative properties do not show temporal or spatial variations, with dust being distributed homogeneously and with a constant dust aerosol particle effective radius of 1.5 microns. Under this assumption of constant radiative properties throughout the atmosphere, the fluxes at the surface and the conversion factor from UV to SW radiation are not affected by the changes in the vertical profile. The effect of including variations in dust particle size is typically below 5% in the UV range (Vicente-Retortillo et al., 2017). The relative effect is expected to be larger during the MY 34 Global Dust Storm, where both dust opacity and particle size were extraordinarily high (Chen-Chen et al., 2020; Lemmon et al., 2019); however, solar fluxes were very small during the GDS (Figure 2b) and therefore the effect on the calculation of other terms of the Surface Energy Budget is small. Finally, uncertainties in SW↓ values were calculated by applying the conversion factor to the uncertainties in the UV_{ABC} measurements (Vicente-Retortillo et al., 2020). The main advantage of using REMS UV-corrected values is that these measurements can reflect diurnal and sol-to-sol variations in atmospheric opacity that were not captured with Mastcam due to the lower measuring frequency, improving the accuracy of the calculated SW fluxes.

When $\theta > 55°$, the simulated UV fluxes were adjusted for each sol using the mean difference between simulations and UV observations with $\theta < 55°$, discarding those hours when this difference was above 10%. That is, when on a given sol there are hours with $\theta < 55°$ for which the difference between both fluxes is smaller

than 10%, we adjust the simulated values with $\theta > 55°$ by the mean of the differences between those fluxes when the difference is below 10%. Alternatively, if on a given sol all the differences for $\theta < 55°$ are above 10%, the threshold was increased to 50% and the adjustment was performed by matching the maximum hourly value based on the UV observations and the corresponding simulated value using COMIMART and Mastcam opacities. We note that the measurements performed when the rover structure is inside the field of view of the sensor (Vicente-Retortillo et al., 2017) are not considered in the adjustment. The relative uncertainties were calculated as the mean relative uncertainties of shortwave values derived from REMS measurements (that is, those with $\theta < 55°$) with the differences below 10%. If there were no values satisfying this condition, relative uncertainties were set to be equal to that at the maximum hourly value for that sol. We note that these uncertainties do not include potential inaccuracies in the aerosol radiative properties and introduced by the plane-parallel assumption for low solar elevations. This second method was also followed for $\theta < 55°$ that presented differences above 10% with respect to simulated values, except for the maximum observed hourly value. The resulting uncertainty in SW↓ is typically below 8% throughout the day, regardless of the season (more details in Section 3.6).

Finally, we note that solar fluxes are not referenced to a horizontal surface but to the rover deck (roughly corresponding to the inclination of the terrain). The median of the hourly values of the rover inclination with respect to a horizontal surface during daytime through the first 2500 sols is ~6.5°, with a maximum value of ~25° and with inclinations above 15° representing around 5% of the total measurements. Except for high solar zenith angles (when the SW radiation term is small), and for extremely high opacities (such as those during the MY 34 GDS), the ratio between fluxes referred to the rover deck and those referred to a horizontal surface, SW_r/SW_h, can be approximated by μ_r/μ_h, where μ represents the cosine of the solar zenith angle. Under this approximation, the relative difference between SW_r and SW_h follows a diurnal cycle, with minimum differences at noon. We obtained that relative differences above 10% represent less than 2% of the sols at 11 and 12 LMST, and 10%, 26%, and 47% of the sols at 10, 9, and 8 LMST, respectively; in general, the differences are smaller during the afternoon.

In summary, variations at a given LMST are not only caused by changes in the Sun–Mars distance, season, and atmospheric dust content, but also by changes in the surface (rover) orientation. However, when averaged throughout the mission, the effect of the rover tilt is smaller than 5% between 8 and 16 LMST.

Finally, we calculated the hourly upwelling reflected solar radiation as SW↑ = α SW↓, where we assumed a Lambertian albedo (radiance equally reflected in every angle). Uncertainties in SW↑ were obtained by quadratically adding those in albedo (0.025) and in SW↓ (more details in Section 3.6).

3.2. Ground Heat Flux

We used MSL/REMS measurements of ground temperature as an upper boundary condition to solve the heat conduction equation in the soil:

$$\frac{\partial T(z,t)}{\partial t} = \left(\frac{I}{\rho c}\right)^2 \frac{\partial^2 T(z,t)}{\partial z^2}; \tag{2}$$

$$T(z = 0, t) = T_g^{REMS}(t); \tag{3}$$

$$T(z = z_d, t) = T_d, \tag{4}$$

where I is the thermal inertia (Figure 4, bottom), ρ the soil density, c the soil specific heat, and z_d the depth at which the subsurface temperature is constant and equal to T_d. The solution to this equation is the vertical profile of subsurface temperature, $T(z, t)$, from which we obtained the ground heat flux as:

$$G(t) = -\left(\frac{I}{\rho c}\right)^2 \frac{\partial T(z,t)}{\partial z}\bigg|_{z=0}. \tag{5}$$

We used the Matlab "pdepe" package to solve Equations 2–5. This package was designed to solve 1-D parabolic and elliptic partial differential equations (PDEs). Nominally, we set the temporal domain to 8 sols and the vertical domain down to 3 times the e-folding penetration depth, where the temperature was set to T_d (Equation 4). We used a vertical step of $\Delta z = z_d/400$ cm and a time step of $\Delta t = 10$ s. Additionally, the initial

profile T(z, $t = 0$) was set to a straight line connecting the observed T_g at 00:00 LMST and T_d, although the results are quite insensitive to this profile. After a spin-up period of about three sols, the package converged toward a stable solution. For each sol, each run takes approximately 10 s under this configuration.

We performed sensitivity studies to the changes in Δz, Δt, and the initial profile T(z, $t = 0$), which resulted in typical variations in G below 1% when Δz, Δt, and T(z, $t = 0$) varied within the same order of magnitude as those used nominally. Furthermore, we compared the performance of the Matlab "pdepe" package with the 5-point Crank–Nicholson soil thermal diffusion scheme used in the University of Helsinki/Finnish Meteorological Institute adsorptive subsurface–atmosphere column model (hereafter called SCM; e.g., Savijärvi and Määttänen, 2010). This comparison yielded excellent results, with differences in simulated ground temperatures <1 K when forced with the same G.

Values of the parameters needed to solve Equations 2–5 were calculated as follows. On each sol, z_d was set to $3 \times L$, where $L = \sqrt{2/\omega}\left(I/\rho c\right)$ is the diurnal e-folding depth (with typical values of a few cm), $\omega = 7.0774 \times 10^{-5}$ s^{-1} is the angular speed of the planet's rotation, and $\rho c = 1.2 \times 10^6$ Jm^{-3}K^{-1} (Martínez et al., 2014; Möhlmann, 2004). Following consistency assessments between our results and those obtained from numerical models (more details in Section 5.1), we set $T_d = 220$ K over the first 2500 sols. To obtain this value, we analyzed the results from several sols. In particular, we focused on two extreme cases: sol 530 (Ls = 84°), with relatively low thermal inertia (200 SI) and daily mean T_g (~209 K) and sol 125 (Ls = 223°), with relatively high thermal inertia (560 SI) and daily mean T_g (~235 K) (Figures 2e and 4, bottom). On sols 530 and 125, respectively, $T_d = 215$ and 225 K provided an excellent match between our results and SCM's, whereas $T_d = 220$ K provided an optimized match on all other sols with less limiting values of thermal inertia and daily mean T_g.

As discussed in Martínez et al. (2014), the solution to Equations 2–5 primarily depends on I, with smaller variations as a function of T_d, z_d, and ρc. Thus, we calculated conservative error bars by considering the uncertainties of ±50 SI units in I (and thus in z_d), ±5 K in T_d, and ±0.4 × 10^6 Jm^{-3}K^{-1} in ρc. This strategy resulted in relative errors around 20% for the calculated hourly G values throughout the mission (more details in Section 3.6).

Finally, we have implicitly assumed a homogeneous soil (Equation 2) to calculate G. However, using THM on a few selected sols, Vasavada et al. (2017) showed that the match between observed and simulated T_g values could be improved during certain periods of the sol when a heterogeneous soil with lateral or vertical variations in thermal inertia was considered. This aspect, which has not been quantified here, has important implications for the physical interpretation of the G and LW↓ values obtained here, as shown in Sections 3.6, 4.2, and 5.1.

3.3. Sensible Heat Flux

The surface sensible heat flux is defined as TF $= \rho_a c_p \left(\overline{w'T'}\right)_s$, where ρ_a is the air density, $c_p = 736$ J Kg^{-1} K^{-1} is the specific heat of CO_2 gas at constant pressure, $\left(\overline{w'T'}\right)_s$ is the covariance between the turbulent departures of temperature, T', and vertical wind speed, w' at the surface. The period over which turbulent departures are calculated is typically of the order of a few to tens of minutes, coinciding with the energy gap in the spectral intensity of wind speed and temperature on Earth and Mars (Banfield et al., 2020; Davy et al., 2010).

Since measurements of the vertical component of the wind speed have not yet been performed on Mars, the covariance term $\left(\overline{w'T'}\right)_s$ cannot be obtained directly. Therefore, we applied the indirect drag transfer method to calculate TF (Savijärvi, 1995; Sutton et al., 1978; Tillman et al., 1994). Following this approach, the sensible heat flux was calculated as:

$$TF = k^2 U_a \rho_a c_p f\left(R_B\right) \frac{\left(T_g - T_a\right)}{\ln^2\left(z_a / z_0\right)}, \tag{6}$$

where $k = 0.4$ is the von Karman constant, $z_a = 1.6$ m is approximately the height at which the air temperature (Figure 2f) is measured, z_0 is the surface roughness (set to 1 cm; Hébrard et al., 2012), and f(R_B) is a function of the bulk Richardson number that accounts for the thermal stability in the near surface of Mars.

We note that MarsWRF provides U_a at 1.5 m every 10 min; however, the differences in the model from 1.5 to 1.6 m are tiny based on single-value calculations. For convective conditions, the applied $f(R_B)$ obeys the correct-free convection limit (Savijärvi and Kauhanen, 2008); for stable conditions, it has been validated under Earth Polar conditions and therefore is reasonably suitable for applications in cold, dry Martian-like environments (Savijärvi and Määttänen, 2010).

Application of our methodology resulted in uncertainties in hourly TF values of about 10%, regardless of the season. They were estimated using uncertainties in T_g and T_a values (of the order of a few K), and in z_0 (0.1–10 cm), and then calculating maximum and minimum values of TF from Equation 6 using extreme values of T_g–T_a and z_0. Additional uncertainties come from using model winds for U_a; however, we could not quantify this effect in the absence of in situ wind data.

3.4. Latent Heat Fluxes

The surface latent heat flux is defined as $LF = \rho_a L_v \left(\overline{w'q'} \right)_s$, where $L_v = 2.8 \times 10^6$ J Kg^{-1} is the latent heat of sublimation for water vapor and $\left(\overline{w'q'} \right)_s$ is the covariance between the turbulent departures of specific humidity, q', and vertical wind speed at the surface. As for TF, LF fluxes cannot be directly measured on Mars due to the lack of measurements of the vertical component of the wind speed. Moreover, while q has been inferred using relative humidity and temperature measurements from the Phoenix and MSL missions (Fischer et al., 2019), the sampling rate and response time of the RH sensors precluded the calculations of q'.

In the absence of direct $\left(\overline{w'q'} \right)_s$ measurements, we calculated LF values by applying the drag transfer method to Mars as:

$$LF = L_v \beta k^2 U_a \rho_a c_p f\left(R_B \right) \frac{\left[q_s \left(T = T_g \right) - q_a \right]}{\ln^2 \left(z_a / z_0 \right)}, \qquad (7)$$

where q_s is the saturation-specific humidity at $T = T_g$, q_a is the specific humidity at z_a, and β is the top-soil moisture availability that ranges between 0 (completely dry) and 1 (saturated soil) (Savijärvi and Määttanen, 2010).

Although frost has been predicted to form at Gale around Ls 90° every Martian year (Martínez et al., 2016) coinciding with annual coldest and most humid conditions (Figures 2e–2g), experimental campaigns conducted around Ls = 90° in MYs 33 and 34 did not detect frost. Experimental results from the latest frost campaign conducted in MY 35 at Ls ~ 100°, when the relative humidity in the air surpassed 100% for the first time (Figure 2g, green squares), indicated that frost might have formed (Gough et al., 2020). However, even if frost forms, LF values can be neglected in the SEB at Gale. By performing a scale analysis of Equation 7 with values of $\rho_a \sim 10^{-2}$ kg m^{-3} (Figure 2d), $q_a \sim 10^{-4}$ (Figure 2h, where q_a = VMR × (R/R$_v$), with $R_v = 461$ kg^{-1} K^{-1} the specific gas constant of water vapor), $U_a \sim 5$ m s^{-1} (Figure 3), $\beta \times f(R_B)$ in the range 0–1, and $1/\ln^2(z_a/z_0) \sim 10^{-2}$, we obtained maximum values of LF of a few tenths of W/m^2 at most. As shown in Section 4, these values are significantly lower than those of the other terms in Equation 1.

3.5. Longwave Fluxes

We calculated the upwelling LW radiation emitted by the surface as $LW\uparrow = \varepsilon \sigma T_g^4$, where $\varepsilon = 0.98$ is the surface emissivity averaged over all thermal infrared wavelengths and σ is the Stefan Boltzmann constant. By considering ε values between 0.96 and 1 (Christensen et al., 2004) and the uncertainties in the derived hourly T_g values (of the order of a few K), we obtained uncertainties in $LW\uparrow$ of less than 8% (more details in Section 3.6).

As the final product, we obtained the downwelling LW radiation from the whole atmosphere as:

$$LW \downarrow = G - SW \downarrow \left(1 - \alpha \right) + LW \uparrow + TF, \qquad (8)$$
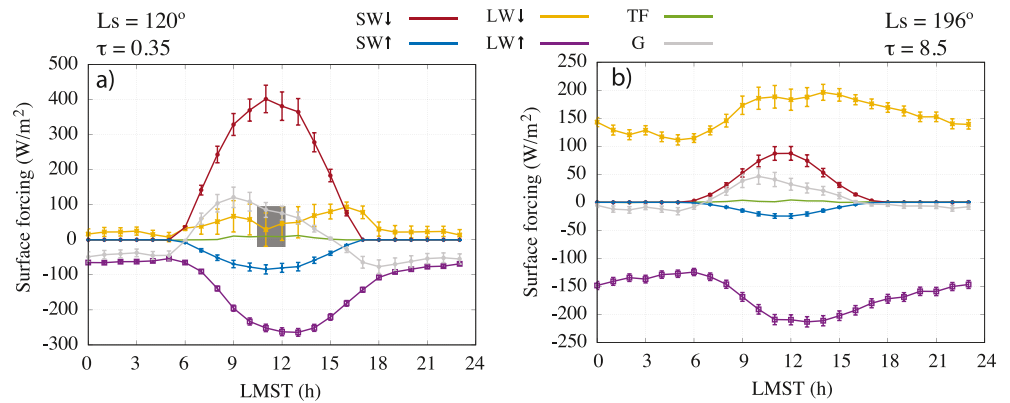
Figure 5. Diurnal variation of the surface energy budget on sols 607 (a) and 2085 (b). The gray-shaded box on the left highlights the hours in which the relative error in LW↑ (yellow line) is >100%. For readability, uncertainties in TF fluxes (green line) have not been added (<10%). Note that y-axis range is different in both figures.

where each term on the right-hand side of Equation 8 was calculated as explained in previous sections. Absolute uncertainties in LW↓ were obtained by quadratically adding those in the various terms in Equation 8. Analyses of these uncertainties and their significance are provided in Section 3.6.

In addition to the uncertainties accounted for in LW↓ derived from the other terms, three simplifications were assumed to obtain LW↓ relative to the methods used for Earth. First, we neglected the storage of internal energy (e.g., chemical storage by photosynthesis) and horizontal flux of energy due to advection in Equation 8. Second, we assumed that all the fluxes in Equation 8 are referenced to a horizontal surface. As explained in Section 3.1, this is a reasonable approximation because the effect of the rover tilt in SW↓ is smaller than 5% between 8 and 16 LMST when averaged throughout the mission. Third, we assumed that the soil is homogeneous within the diurnal penetration depth (Equations 2–5) and with no lateral variations in thermal inertia, which likely affect the obtained values of G (and thus LW↓) at certain times of the sol (more details in Sections 3.6, 4.2, and 5.1).

3.6. Uncertainties

To exemplify the significance of the obtained uncertainties while postponing scientific analyses to Section 4, we show in Figure 5 the diurnal evolution of each term of the SEB and its corresponding error on sols 607 (Ls = 120°, τ = 0.35) and 2085 (Ls = 196°, τ = 8.5). We chose these two sols to show extreme scenarios for LW↓, corresponding to the clearest and dustiest atmosphere, respectively (Figure 2a). On sol 607 (Figure 5, left), as well as on the vast majority of the sols on which we have calculated the SEB, the most relevant aspects are that LW↓ (yellow line) presents relative errors >100% between 11 a.m. and noon (gray-shaded rectangle) and that the diurnal variation in LW↓ shows an unexpected local maximum in the 7–10 LMST period. As explained in Section 5.1, we attribute this "am" peak to uncertainties arising from assuming a homogeneous soil.

To provide a broader context for the obtained uncertainties, we show in Figure 6 seasonal averages of the hourly relative error in the various terms of the surface energy budget. Relative errors in SW↓ (Figure 6a) and SW↑ (Figure 6b) stay below 8% and 21%, respectively. The relative error in LW↑ presents a strong diurnal variation (Figure 6c), with largest values occurring at the coldest temperatures (nighttime hours in northern spring and summer) due to electronic noise in the GTS. The relative error in G (Figure 6d) is ~20%, regardless of the season and time of the day, except for the peaks in the 06:00–07:00 and 16:00–17:00 periods due to G values being close to 0 W/m².

Among all the SEB terms, LW↓ presents the largest relative error (Figure 6e) because it is calculated by quadratically adding the uncertainties in each of the other terms (Equation 8). This results in relative errors >100% around noon during most of the year, except during the northern fall (yellow line) when atmospheric temperatures are highest (Figure 2f) and atmospheric dust contents are largest (Figure 2a).
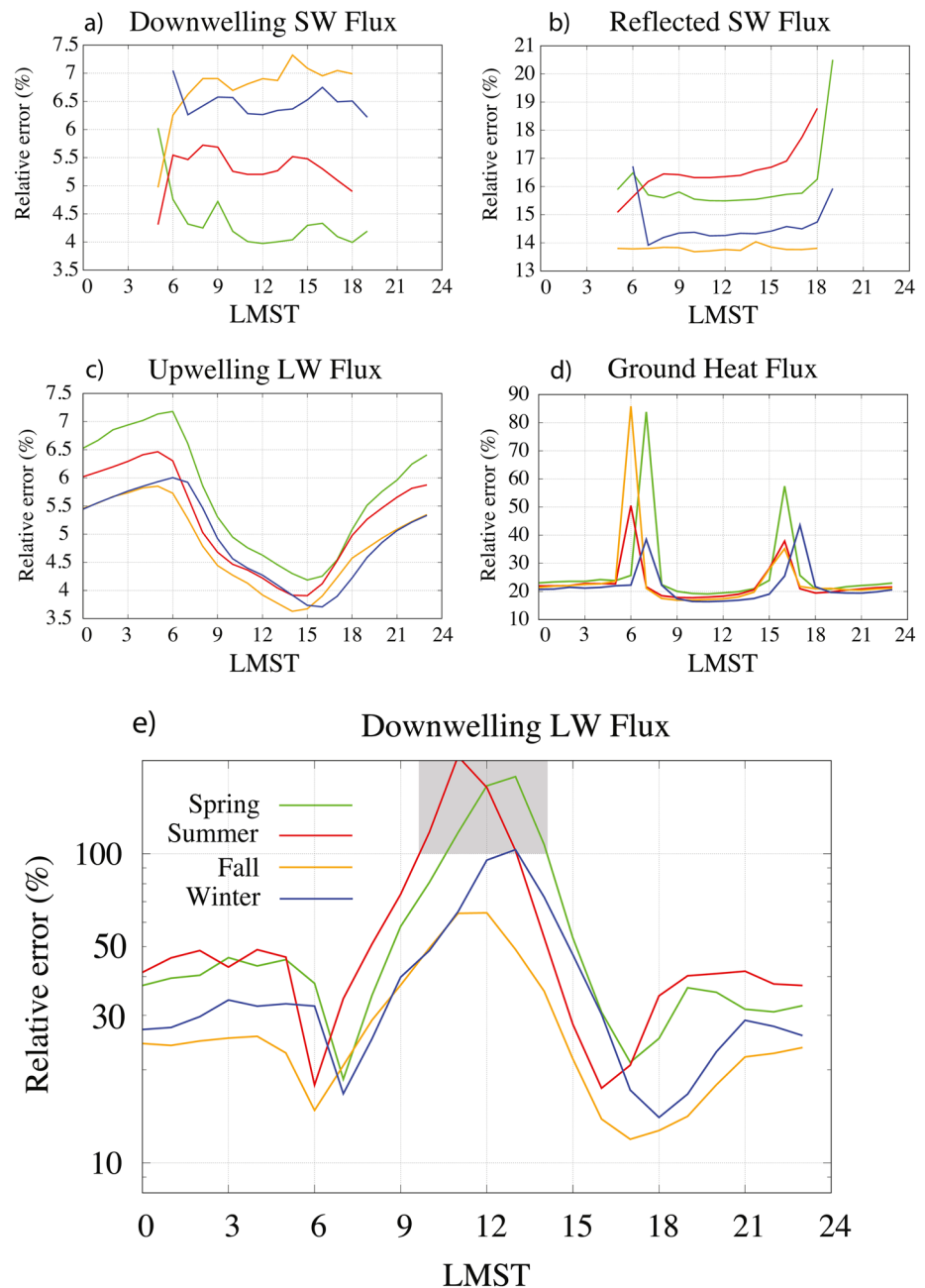
Figure 6. Seasonal average of the hourly relative error of the various terms of the surface energy budget. The gray-shaded box in (e) highlights the hours in which the relative error in LW↓ is >100% (*y*-axis in log scale).

4. Interannual, Seasonal, and Diurnal Variation of the SEB

In this section, we analyze the variation of each term of the SEB from diurnal to interannual timescales. We use the environmental conditions measured at Gale (Figure 2) as a reference to understand the processes causing such variations.

4.1. Shortwave Flux

The interannual and seasonal evolution of SW↓ is shown in Figure 7a. While, during the aphelion season ($Ls = 0°–180°$), the interannual variability is small, it significantly increases during the perihelion season
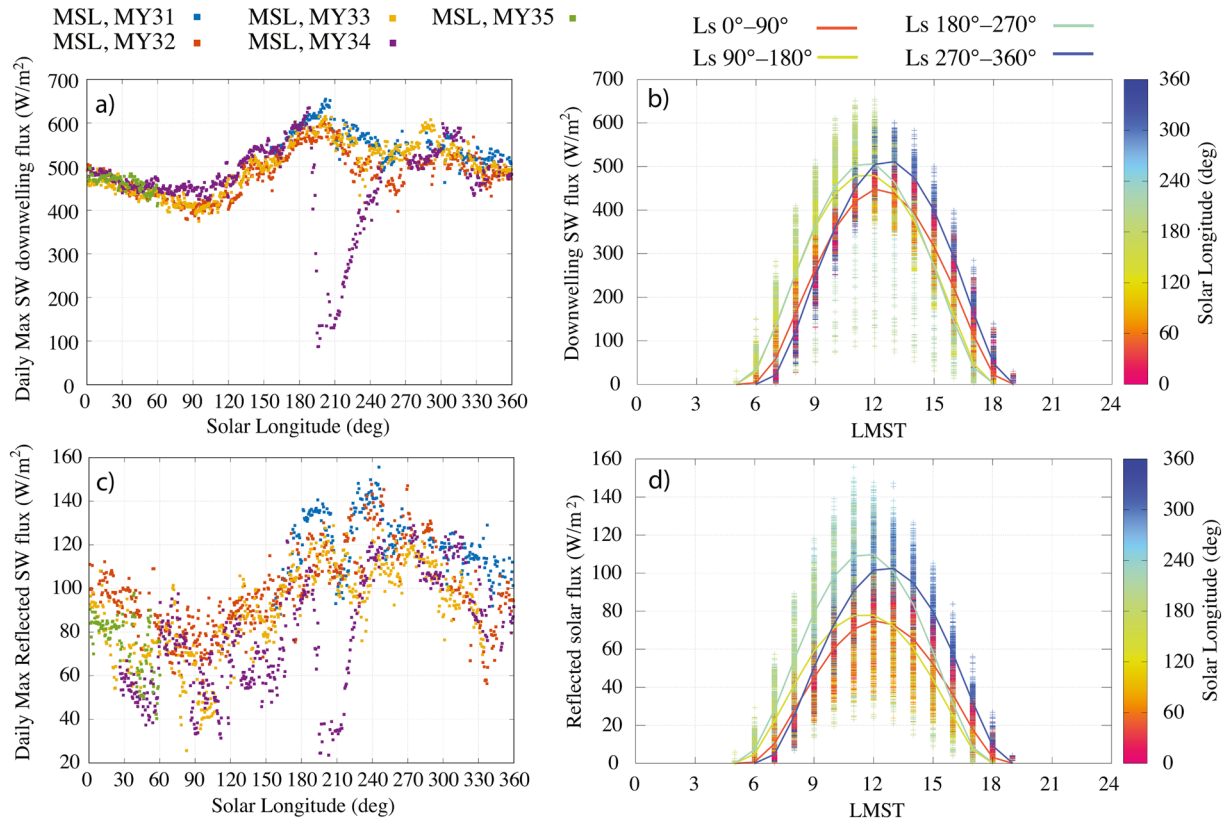
Figure 7. (a) Interannual and seasonal variation of the daily maximum SW↓ as a function of Ls using color code for different MYs. (b) Diurnal variation of SW↓ as a function of LMST using color code for Ls. For reference, the thick, colored lines represent seasonal hourly averages. (c–d) Same as (a–b), but for SW↑. In Figures 7b and 7d, the lowest hourly values appearing in green colors correspond to the MY34 global dust storm.

(Ls = 180°–360°) following interannual changes in dust opacity (Figure 2a). The most extreme example is the MY 34 global dust storm, when the maximum SW↓ flux was reduced by about 90% compared to previous years (Figure 7a, purple squares at Ls ~ 195°). In addition to global dust storms, periods of enhanced dust activity occurring every year between Ls 150° and 170°, 210° and 240°, and 320° and 340° (Figure 2a) caused significant interannual variability in the maximum SW↓ flux (Figure 7a).

The seasonal variation in the maximum SW↓ flux is modest at the near-equatorial latitude of Gale crater (4.6°S), having changes with respect to the annual mean below 20% except in MY 34 (Figure 7a). The annual minimum occurs at Ls ~ 90° between the time of the minimum at the top of the atmosphere (Ls ~ 82°; not shown) and the annual minimum in atmospheric dust opacity (Ls ~ 125°; Figure 2a), while the annual maximum occurs at Ls ~ 200°, prior to the peak at the top of the atmosphere (at Ls ~ 230°; not shown) and while atmospheric dust opacities are still relatively low (Figure 2a).

The diurnal variation of SW↓ is shown in Figure 7b, where colored lines representing seasonal hourly averages were added for reference. The daily maximum SW↓ does not always occur at noon because the differences between LMST and Local True Solar Time present seasonal variations, with maximum values occurring between Ls 270° and 360° (when noon occurs up to 50 min after 12:00 LMST; blue colors) and minimum values between Ls 90° and 180° (when noon occurs up to 40 min before 12:00 LMST; green colors). In addition, diurnal variations in dust opacity and rover tilt can also lead to asymmetric variations in the solar flux with respect to 12:00 LMST. These three factors explain higher afternoon values during Southern summer (blue colors) and higher morning values during Southern winter (green colors).

The interannual and seasonal evolution of SW↑ is shown in Figure 7c, while its diurnal evolution is shown in Figure 7d. Following strong sol-to-sol variations in albedo (Figure 4, top), the interannual and sol-to-sol variability in SW↑ (Figure 7c) is significantly larger than that in SW↓ (Figure 7a). Also, the seasonal
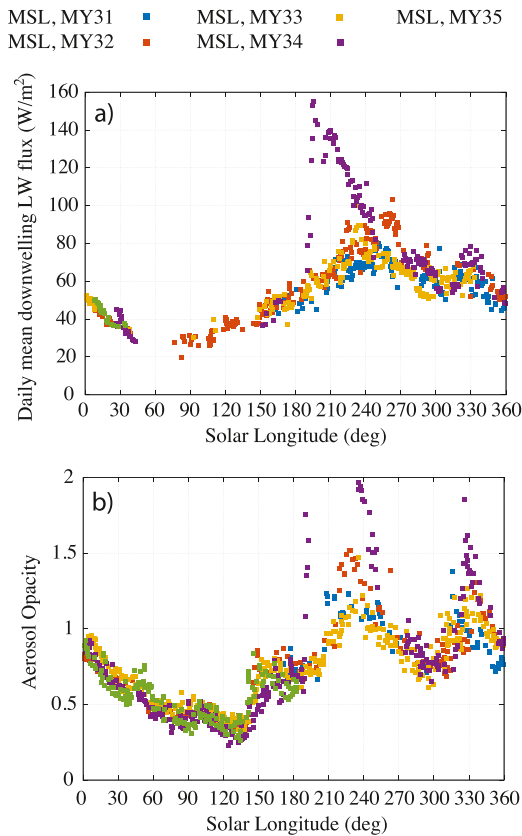
Figure 8. (a) Interannual and seasonal variation of the daily mean LW↓ flux during the first 2500 sols of the MSL mission. The daily mean LW↓ is only shown for sols with full diurnal coverage. (b) As in Figure 2a, but with the *y*-axis range between 0 and 2 to magnify dust variation outside the global dust storm in MY 34.
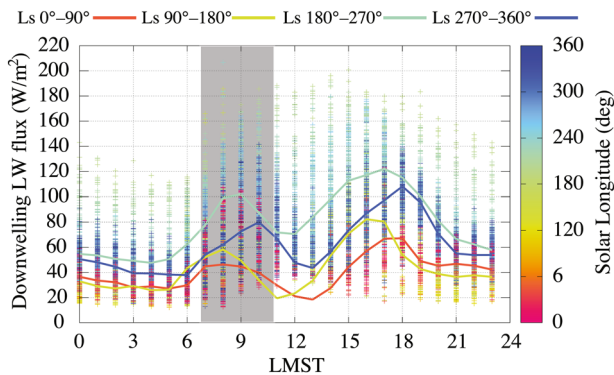

Figure 9. Diurnal variation of LW↓ as a function of LMST using color code for Ls. For reference, the thick, colored lines represent seasonal hourly averages LW↓ flux. The gray-shaded box highlights the 7–10 LMST peak occurring in every season, which likely arises from the assumption of a homogeneous soil and therefore is not real.

variation of the daily maximum SW↑ flux is larger than that of SW↓, having changes with respect to the annual mean up to ∼35% (vs. ∼20% for SW↓). This is because, on average, both the albedo and SW↓ fluxes are larger during the perihelion than during the aphelion season. Understanding seasonal changes in albedo is outside the scope of this article, but some discussion is provided in Section 5.

4.2. Longwave Flux

The downwelling atmospheric LW flux at the Martian surface depends on the vertical profiles of dust and temperature in a rather complex fashion (Savijärvi, 2014). Unfortunately, such profiles cannot be measured by Curiosity. Therefore, we use measured column abundances of dust and near-surface air temperatures at 1.6 m (Figures 2a and 2f) for comparisons.

The interannual and seasonal variability of the daily mean LW↓ is shown in Figure 8a. To facilitate comparisons, Figure 8b shows dust opacity values as in Figure 2a, but with the *y*-axis range set between 0 and 2 to magnify variations outside MY 34. The daily mean LW↓ is only shown for sols with full diurnal coverage. We note that hourly values of LW↓ were obtained from Equation 8, and therefore its temporal coverage is limited by that of each of the other SEB terms.

Although the interannual variability of the daily mean LW↓ cannot be assessed with enough confidence for the entire aphelion season (Ls = 0°–180°), it is small when there is interannual overlap of LW↓ data in Ls (Figure 8a). During the perihelion season, when the temporal coverage is richer, the interannual variability is greater as it is significantly affected by changes in atmospheric dust abundances. In fact, each relative maximum of opacity (Ls ∼195° and ∼325° in MY 34; Ls ∼235° and ∼325° in MY 33; Ls ∼225°, ∼265°, and ∼335° in MY 32; and ∼320° in MY 31; Figure 8b) coincided with a relative maximum of the daily mean LW↓ (Figure 8a), provided that there is a temporal overlap between both quantities (which occurs for each opacity peak except for those at Ls ∼325° in MY 33 and at Ls ∼335° in MY 32). In MY 31, the sparse coverage complicates assessments of the correlation between both quantities.

Interestingly, while dust opacity is slightly declining each MY between 90° and Ls∼135° (Figure 8b), the daily mean LW↓ appears to increase slightly from Ls∼90° in MYs 32 and 33 (Figure 8a). Therefore, changes in dust opacity drive variations in the daily mean LW↓ only during the perihelion season, while changes in daily mean near-surface air temperature values (Figure 2f), with an annual minimum at Ls∼90°, seem to be more correlated with variations in the daily mean LW↓ during the aphelion season. Given uncertainties in daytime LW↓ values (Figure 6e), we have calculated nighttime to check the robustness of this correlation. We obtained the same temporal pattern, with daily and nighttime LW↓ means showing peaks at the same Ls.

The diurnal variation in LW↓ is shown in Figure 9 and presents two local maxima, with a first peak in the 7–10 LMST period and a second in the 15–19 LMST period. This behavior is completely unexpected, as numerical models such as the SCM and THM or the Mars Climate Database (MCD) (Forget et al., 1999; Madeleine et al., 2011) built using the LMD Martian Atmospheric General Circulation Model predict only the
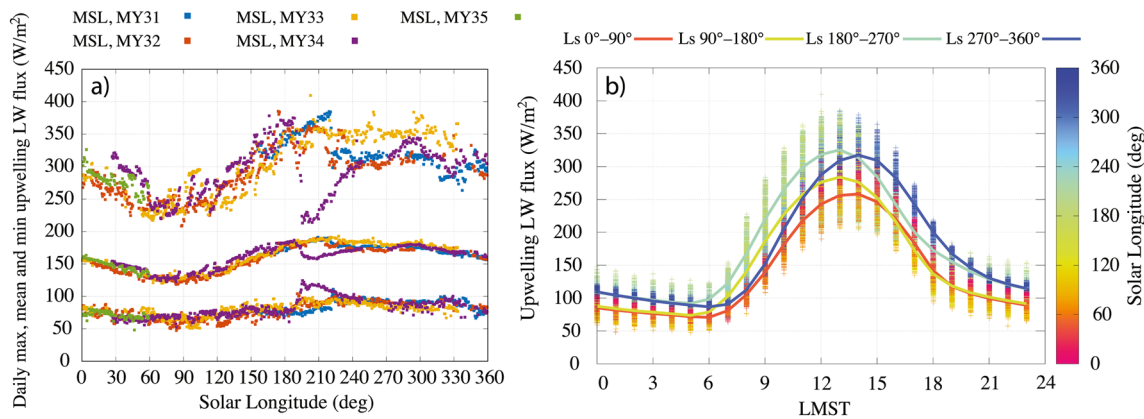
Figure 10. (a) Interannual and seasonal variation of the daily maximum, mean, and minimum LW↑ flux during the first 2500 sols of the Mars Science Laboratory mission. (b) Diurnal variation of LW↑ as a function of Local Mean Solar Time using color code for Ls. For reference, the thick, colored lines represent seasonal hourly averages of the LW↑ flux.

15–19 LMST peak following dust emission from the Sun-heated late afternoon air column (e.g., Savijärvi et al., 2020). While the 7–10 LMST peak in LW↓ may be due to its large relative error (~20%–100% depending on Ls; Figure 6d), the two maxima exist for the vast majority of the sols, regardless of the season, environmental conditions, and types of terrains traversed by the Curiosity rover. This led us to assess the consistency between our results and those obtained from numerical models. Analyses of this assessment are presented in Section 5.1 and indicate that the 7–10 LMST peak likely arises from the assumption of a homogeneous soil, in addition to the uncertainties already accounted for in LW↓.

The interannual and seasonal variability of the daily maximum, mean, and minimum LW↑ is shown in Figure 10a and follows changes in ground temperature (Figure 2e) by definition (LW↑ = $\varepsilon\sigma T_g^4$). Outside the global dust storm in MY 34 (purple squares), interannual variations are modest over all Ls. An exception to this occurred in MY 33 (yellow squares) between Ls 120° and 180°, when the daily maximum (minimum) was consistently lower (higher) than in other MYs, and between Ls 210° and 330°, when the daily maximum (minimum) was consistently higher (lower). This behavior was caused by relatively higher (Ls 120°–180°) and lower (Ls 210°–330°) values of thermal inertia compared to other MYs (Figure 4b), causing daily maximum (minimum) ground temperatures in MY 33 between Ls 120° and 180° to be colder (warmer) than in other MYs, and between Ls 210° and 330° to be warmer (colder) than in other MYs.

As for the ground temperature (Figure 2e), the seasonal variation in the daily maximum, mean, and minimum LW↑ flux is modest at the near-equatorial latitude of Gale, with an annual maximum at Ls~210° and an annual minimum at Ls~85° (Figure 10a). Note that these annual peaks are almost contemporaneous to those in SW↓, which occur at Ls~200° and 90°, respectively (Figure 7a).

Figure 10b shows the diurnal variability of LW↑, with maxima at 13 LMST in Ls 90°–270° (green and turquoise lines) and at 14 LMST in Ls 270°–90° (blue and red lines), and with minima at 5 a.m. in Ls 90°–270°, and at 6 a.m. in Ls 270°–90°. The diurnal maximum is roughly achieved one hour later than that in SW↓, while the diurnal minimum coincides with sunrise (Figure 7b).

4.3. Ground Heat Flux

The interannual and seasonal variability of the daily maximum, mean, and minimum G values is shown in Figures 11a. When averaged over a full diurnal cycle, the daily mean ground heat flux is close to zero throughout the year, although it slightly presents negative values in Ls~30°–120°, with a minimum of ~ -5 W/m² at Ls~90°, and slightly positive values the rest of the year, with a maximum of 18 W/m² at Ls ~ 210°. Outside the global dust storm in MY 34, interannual and seasonal variations in G are modest as a function of Ls and are primarily caused by changes in thermal inertia.

Figure 11b shows the diurnal variability of G, with maxima at 9 LMST in Ls 90°–270° (green and turquoise lines) and at 11 LMST in Ls 270°–90° (blue and red lines). Therefore, the ground heat flux peaks, on average,
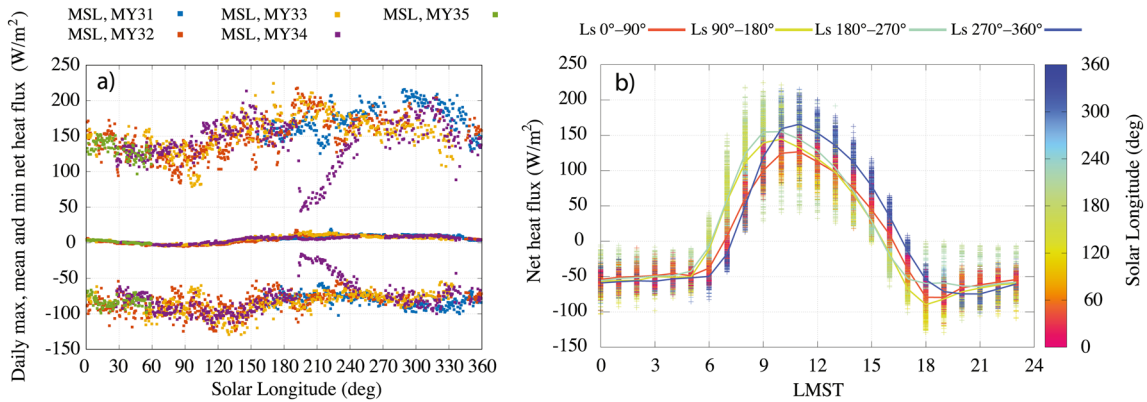
Figure 11. (a) Interannual and seasonal variation of the daily maximum, mean, and minimum ground heat flux during the first 2500 sols of the Mars Science Laboratory mission. (b) Diurnal variation of the ground heat flux as a function of Local Mean Solar Time using color code for Ls. For reference, the thick-colored lines represent seasonal hourly averages of (g)

four hours prior to the ground temperature between Ls 90° and 270° and three hours before between Ls 270° and 90° (Figure 10b). Then, the ground heat flux turns negative (conduction from the subsurface up to the surface) from ~15.30 to ~06:00 LMST in Ls 90°–270° and from ~16:30 LMST to ~07:00 LMST in Ls 270°–90°, stabilizing the shallow subsurface layer at diurnal timescales.

The net heat flux available for conduction into the soil determines the thermal environment in the shallow subsurface, and therefore accurate values of G are critical to simulate subsurface temperatures. As an example, Figure 12 shows the diurnal evolution of subsurface temperatures on sols 124 (solid lines) and 534 (dashed lines), corresponding, respectively, to time periods with annual warmest (Ls = 224°) and coldest (Ls = 85°) daily mean ground temperatures (Figure 2f), and with extreme values of thermal inertia (560 and 180 SI units; Figure 4b). To show the diurnal amplitude at the surface, subsurface profiles are plotted, among others, at the coldest (05:00; blue) and warmest (13:00; red) times of these sols. Note that larger thermal inertia values result in deeper penetration depths and lower diurnal amplitudes at the surface. These results are relevant for Curiosity's drill samples, which come from a depth of 2–6 cm (Vaniman et al., 2018), and to further assess the potential for brine formation (Rivera-Valentín et al., 2018) and habitability of the subsurface of Gale (Rivera-Valentín et al., 2020).
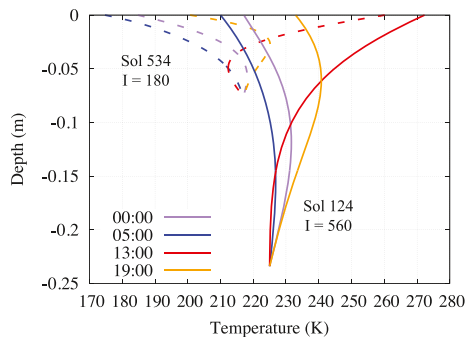
4.4. Sensible Heat Flux

The interannual and seasonal variability of the daily maximum, mean, and minimum TF is shown in Figure 13a. Given low values of atmospheric density (Figure 2d), daily maximum values of TF are at least one order of magnitude lower than those of the other SEB terms (except for LF). The sol-to-sol variability in the daily maximum TF is strong through its dependence on T_g–T_a (Equation 6), which in turn depends on the sol-to-sol variability in the geophysical properties of the terrain (e.g., thermal inertia; Figure 4b) and dust opacity (Figure 2a).

The diurnal variation in TF is shown in Figure 13b, with positive values between sunrise and sunset when $T_g > T_a$, and negative values at nighttime following the development of a thermal inversion ($T_a > T_g$) in the first meters of the atmosphere (Savijärvi and Kauhanen, 2008; Smith et al., 2004). TF daytime values are significantly larger than nighttime values due to larger thermal gradients in the first 1.6 m, with annual average values of +25 K near noon versus −5 K through nighttime (Figures 2e and 2f).

Figure 12. Shallow subsurface temperature profiles on sols 124 (solid lines) and 534 (dashed lines). These two sols correspond to extreme scenarios with the annual warmest and coldest daily mean ground temperatures (Ls = 224° and Ls = 85°), and relatively large and low thermal inertia values (560 and 185 SI), respectively.
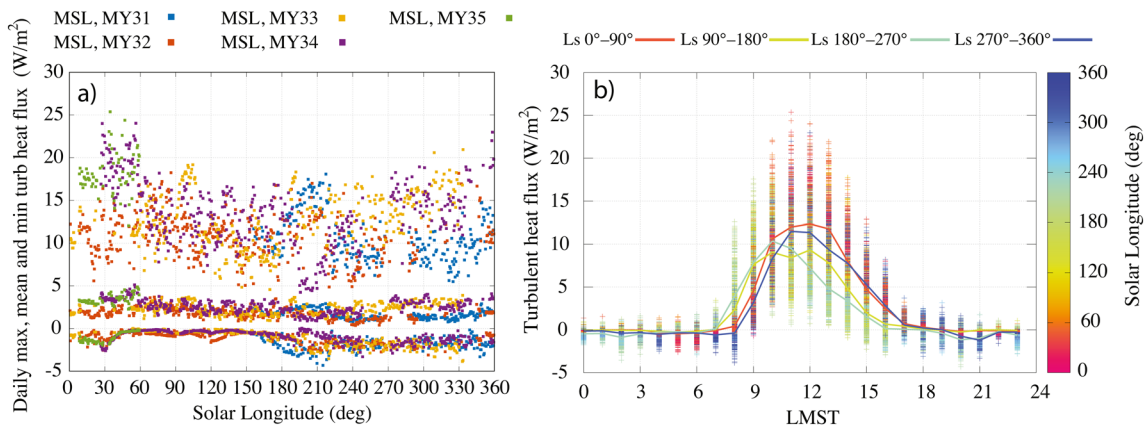
Figure 13. (a) Interannual and seasonal variation of the daily maximum, mean, and minimum sensible heat flux during the first 2500 sols of the MSL mission. (b) Diurnal variation of the sensible heat flux as a function of Local Mean Solar Time using color code for Ls. For reference, the thick, colored lines represent seasonal hourly averages of TF.

Interestingly, seasonal averages of TF, represented by the colored solid lines in Figure 13b, show larger near-noon values between Ls 270° and 90° (red and blue lines) than between Ls 90° and 270° (green and turquoise lines). This behavior is caused by strong seasonal variations in air density, with larger values in Ls 270°–90° than elsewhere in the year (Equation 6 and Figure 2d). Although not shown here, near-noon measured (T_g - T_a) and simulated U_a do not show a marked seasonal variation and therefore do not significantly affect seasonal variations in TF. A more in-depth discussion of TF and its variability on different timescales in relation to convective activity over Curiosity rover's traverse is presented in Section 5.2.

5. Discussion

5.1. Consistency Assessment With Modeling

The unexpected diurnal peak in LW↓ in the 7–10 LMST period (Figure 9), which is not predicted by numerical models, led us to assess the consistency between our results and those obtained from SCM and THM. We choose results from sol 895 (Ls ∼ 289°) to establish comparisons between our results and models. On other sols, analyses of these comparisons yielded similar conclusions, both qualitatively and quantitatively.

Starting with comparisons between models, ground heat fluxes (and thus the SEB terms on the right-hand side of Equation 1) simulated by SCM and THM are in very good agreement when the parameters used to initialize both models are the same (e.g., column opacity, albedo, or thermal inertia). As an example, Figure 14a shows that maximum departures between the two models on sol 895 range between ∼5 W/m² during nighttime (i.e., relative differences <∼10%) and ∼10 W/m² during daytime (i.e., relative differences <∼6%). Thus, we only show SCM-derived values in the remainder of this section.

Figure 14b shows the observed (red) and SCM-simulated (black line) ground temperature on this sol. While SCM provides a very good match to observed T_g in early a.m., near noon and late p.m. local times, it underestimates T_g after sunrise and before sunset (similar to THM; see Figure 14 in Vasavada et al., 2017). This behavior is key to understand Figure 14c, which shows the SEB as obtained in this article (colored symbols) and as simulated by SCM (colored lines).

Within uncertainties, SW↓ (brown) and SW↑ (blue) are in very good agreement. Since the rover deck was tilted (∼8°) roughly toward the North (pointing azimuth = −3.58°, with 0° indicating North), REMS/UVS-derived SW↓ fluxes are slightly lower than those simulated on a flat surface throughout the sol. Of most importance, the largest departures are found in LW↑ (=$\varepsilon\sigma T_g^4$; purple), G (gray), and LW↓ (yellow) during the periods in which SCM underestimates T_g (after sunrise and before sunset). In particular, the largest relative departures are found in LW↓ because SCM does not predict the "a.m" peak after sunrise and because the simulated "p.m" peak is lower than in our results. We note that the same behavior is found in simulations performed with THM and results from MCD.
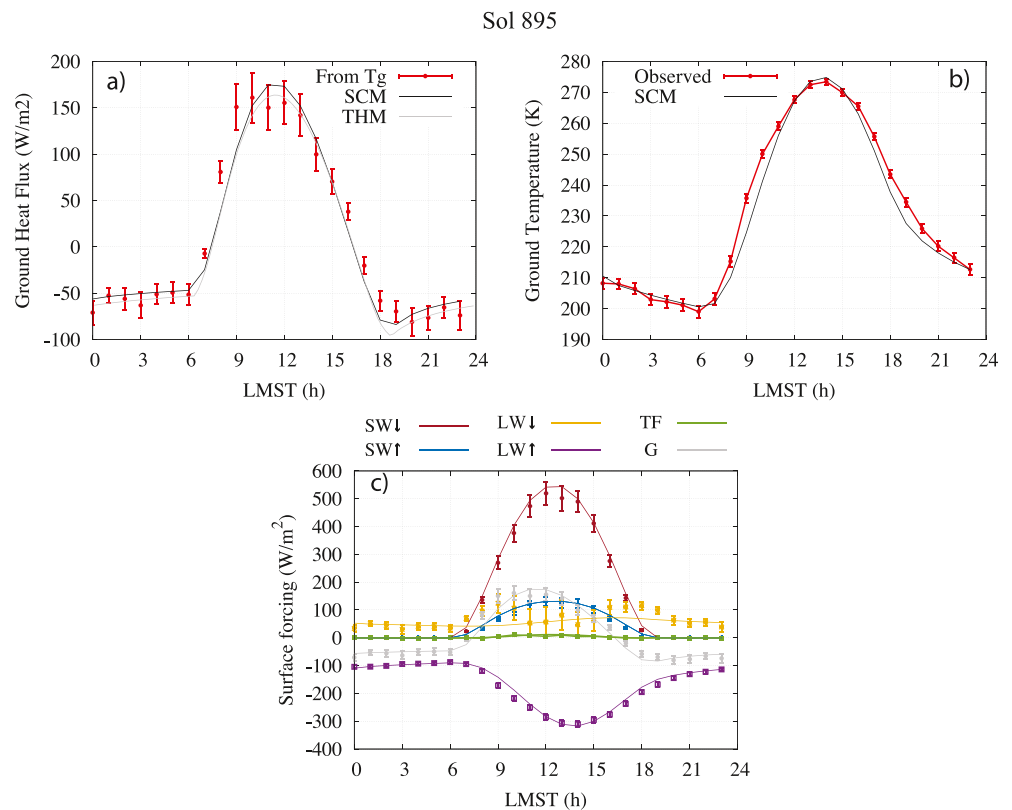
Figure 14. (a) Ground heat flux values on sol 895 (Ls ∼ 289°) obtained from ground temperature measurements as described in Section 3.2 of the manuscript (red) and simulated by SCM (black line) and THM (gray line). Both models were run using values of column opacity = 0.9, albedo = 0.25, thermal inertia = 380 SI, $\rho c = 1.2 \times 106$ Jm^{-3}K^{-1}, and surface emissivity = 0.98. (b) Observed (red) and SCM-simulated (black) ground temperature values on sol 895. (c) Surface energy budget on the same sol obtained as described in Section 3 (symbols) and simulated by SCM (lines).

After careful considerations, including further comparisons on other sols with variations in Ls, column opacity, rover tilt, rover pointing azimuth, albedo, and thermal inertia values [e.g., sols 30–37 (Bradbury), 125, 191, 391, 530, 770, 1130 (Stimson), 1222 (Namib dune)], we concluded that our results for *G* (and thus LW↓) are likely affected by the assumption of a homogeneous soil (Equation 2). We have reached this conclusion because: (1) REMS/UVS-derived and modeled SW fluxes are generally in good agreement, (2) we have run SCM and THM under different configurations (including enhanced near-surface dust in a.m. hours) and analyzed results from MCD using different "dust scenarios," but these models could not simulate this peak based on first principles, and (3) surfaces with lateral or vertical variations in thermal inertia exhibit distinct phasing at the times of most rapid warming/cooling, coinciding with the periods when observed and SCM-simulated ground temperature depart (Figure 14b). In fact, using THM, Vasavada et al. (2017) showed that the match between observed and simulated T_g values could be improved after sunrise and before sunset (Section 5 of that article) when a heterogeneous soil was considered.

Therefore, the most likely scenario is that our results for *G* (and thus LW↓) are affected after sunrise and before sunset by the assumption of a homogeneous soil, which would explain the unexpected "a.m" peak and the "too-large-pm" peak in LW↓ (Figure 9). Finally, we note that to quantify uncertainties derived from assuming a heterogeneous soil in a systematized, hourly fashion, heterogeneities in the field of view of the REMS/GTS would need to be inspected visually, sol by sol, across Curiosity's traverse. Thus, this is left as future work.
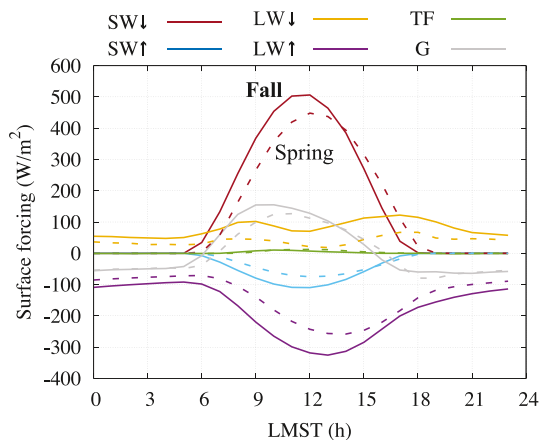
Figure 15. Diurnal variation of the seasonally averaged surface energy budget at Gale in the northern Fall (Ls 180°–270, solid lines) and Spring (Ls 0°–90, dashed lines). Given relatively low values of TF (green line) and LF (not shown) as compared to other surface energy budget terms, the Martian surface energy budget is almost purely radiatively driven.

5.2. Significance of Each SEB Term at Gale

Figure 15 shows seasonally averaged hourly values of the surface energy budget in the northern Fall (Ls 180°–270°, solid lines) and Spring (Ls 0°–90°, dashed lines), corresponding to the dustiest and warmest, and clearest and coldest seasons at Gale, respectively (Figures 2a and 2e). Regardless of the season, the downwelling solar flux (brown) is the primary surface forcing (positive values), showing a modest seasonal variation given the near-equatorial latitude of Gale. The atmospheric LW radiative forcing (yellow) is typically one order of magnitude lower than the solar forcing, and during the dustiest season (solid line), it shows values twice as large as during the clearest season (dashed line). The surface upwelling LW flux (purple) is smaller than the downwelling solar flux, but still of the same order of magnitude, while the reflected solar radiation (light blue) is one order of magnitude smaller, given albedo values (Figure 4a).

The combination of these four terms (up- and downwelling SW and LW fluxes) comprises the net radiative forcing of the surface (R_{NET} = SW↓(1 − α) + LW↓ − LW↑). Because the latent heat flux (not shown) and the sensible heat flux (green) contribute the least to the SEB due to, respectively, the low water content and low density of the Martian atmosphere (Figures 2h and 2d), the ground heat flux (gray) virtually accounts for the entire net radiative forcing. Specifically, whereas on a clear day over land on Earth, the ground heat flux is around 10% of the net radiative forcing during daytime, and around 50% at night (Stull, 2012), at Gale the estimated ground heat flux is ∼95% of the net radiative forcing during the daytime, and around 99% at night, with TF accounting for the remainder. Hourly values of each term of the SEB, except for LF, are available in the repository of the Lunar and Planetary Institute as indicated in the acknowledgments.

5.3. Open Questions

5.3.1. Seasonal Variability of Albedo

Albedo values shown in Figure 4 were derived indirectly by fitting the diurnal temperature curve using the methods and model described in Vasavada et al. (2017). Interestingly, these values peak between Ls ∼ 210° and 270° every MY, coincident with the peak in aerosol opacity (Figure 2a). One explanation is that a dust coating temporarily brightens surfaces within Gale during this season. Albedo measurements of other regions of Mars from orbit have noted significant, transient increases in albedo tied to settling of atmospheric dust (Szwast et al., 2006). Without an independent measurement of albedo at solar wavelengths, however, we are unable to rule out a deficiency in the modeling approach (e.g., incompletely accounting for suspended dust) as the cause of the seasonal peak. Additional analyses of the rover's observations (e.g., examining imaging to infer the variation of dust cover) and modeling approach would be required to fully understand the causes of the seasonal peak.

At other landing sites, the albedo has been inferred from radiometric analyses of images taken by rovers and landers (Bell et al., 2008; Smith et al., 2009), but not in a continuous fashion that would allow analyses of its seasonal variation. The Mars Environmental Dynamics Analyzer (MEDA) onboard the Mars 2020 Perseverance rover is the first instrument to directly measure the incoming and reflected solar radiation on the surface of Mars, allowing direct calculations of the Lambertian albedo and its variations at different timescales (Rodriguez-Manfredi et al., 2020; Sebastian et al., 2020). Given the geometric characteristics of the MEDA instrument and the variations in the slope of the terrain to be traversed by the Perseverance rover, the solar radiation will be measured for a variety of incoming and reflected pairs of angles, allowing the Lambertian assumption to be tested.

5.3.2. Relation Between Sensible Heat Flux and Convective Vortex Activity

Convective vortices occur when buoyantly unstable vertical atmospheric temperature gradients develop near the surface–atmosphere interface of a planetary body. Across Curiosity's traverse, convective vortices

have been inferred from short-lived pressure drops (of the order of tens of seconds) measured by the REMS pressure sensor (Kahanpää et al., 2016; Newman et al., 2019; Ordóñez-Etxeberria et al., 2018, 2020; Steakley and Murphy, 2016). Occasionally, dust devils (i.e., convective vortices containing dust) have been imaged by the Mastcam and Navcam instruments (Newman et al., 2019).

Understanding the formation of convective vortices is important because dust devils are thought to be one of the primary phenomena injecting dust into the Martian atmosphere (Basu et al., 2004; Ferri et al., 2003; Kahre et al., 2006). Renno et al. (1998) developed a simple theory to model dust devils through a parameter referred to as "dust devil activity" (DDA), which depends on the product of TF with the vertical thermodynamic efficiency of the atmosphere (the latter depending on the thickness of the Planetary Boundary Layer).

Using MarsWRF run at a grid spacing of ∼1.4 km, combined with the theory described in Renno et al. (1998), Newman et al. (2019) predicted that greater DDA in MY 33 and 34 as the rover climbed Mons Aeolis was caused primarily by increased (simulated) TF, rather than by increased (simulated) vertical thermodynamic efficiency, with thermal inertia changes over the mission being a secondary effect. Alternatively, Ordóñez-Etxeberria et al. (2020) suggested that the observed increase in pressure drops over the first 2224 sols of the mission (MY 34 and Ls 284°) to either lower thermal inertia favoring larger daytime surface-to-air temperature differences (resulting in larger TF) or to larger thermodynamic efficiencies (i.e., PBL heights).

In the light of new TF values obtained in Section 4 using REMS measurements, in combination with new pressure drops measured by REMS during through sol 2500, we assess below the role of TF, (T_g-T_a), and thermal inertia in the development of convective vortices as measured by REMS. Figure 16a shows the temporal coverage of pressure drops as a function of sol number and LMST, with color code used for Ls and bubbles of different sizes used for the intensity of such pressure drops. Figures 16b–16d show, respectively, contemporaneous values of TF, T_g–T_a, and thermal inertia as a function of sol number, with color code used for MY. Interestingly, there is no clear correlation between TF and the number and intensity of convective pressure drops. While in MY 33 and 34 between Ls∼270° and 315°, the number and intensity of convective pressure drops peaked (shaded area in Figure 16a), the corresponding TF and T_g-T_a (and thermal inertia) were not significantly larger (lower) than in previous MYs in other Ls periods (shaded area in Figures 16b–16d).

Therefore, increases in vortex activity as measured by REMS cannot be explained only by enhanced TF values (nor by increases in T_g–T_a following a reduction in thermal inertia). This suggests that increases in thermodynamical efficiency (PBL thickening) as the rover ascends Aeolis Mons might play an important role in the development of vortices. We note, though, that TF values obtained in this article are "local," as they have been calculated using thermal inertia and ground temperature values representative of the REMS/GTS field of view, whereas those in Newman et al. (2019) were obtained at larger spatial scales using thermal inertia values derived from orbital data sets and may be more representative of the wider region over which vortices detected by REMS were generated.

In future work, we plan to compare the results shown here with those presented in Newman et al. (2019) to understand discrepancies in correlations between DDA (through pressure drops) and TF values originated by the use of different spatial scales. Given the far greater importance of radiative versus sensible heating on Mars compared to Earth (for which the DDA theory was developed), work is also ongoing to include this effect into the DDA calculations. However, it should be noted that the relative contribution of radiative versus sensible heating to the surface energy balance is not representative of the relative contribution to heating of the near-surface atmospheric layer responsible for driving convective vortex formation. Indeed, recent calculations show that the sensible heat contribution to atmospheric heating of the lowest tens of meters of the atmosphere is between 40% and 50% that of LW heating, with the vast majority of the upward LW heat flux from the surface passing through this atmospheric region unabsorbed (Wu et al., 2021).

Furthermore, we plan to analyze our results and pressure drops in relation to those obtained by the InSight mission (Spiga et al., 2020), based on which the vortex encounters were much more correlated with the ambient wind speed (they were advected) than with local values of sensible heat flux and surface-to-atmosphere temperature gradients (Spiga et al., 2020). This was potentially an "observer effect" in which more vortices were simply advected over the pressure sensor per hour when wind speeds increased.
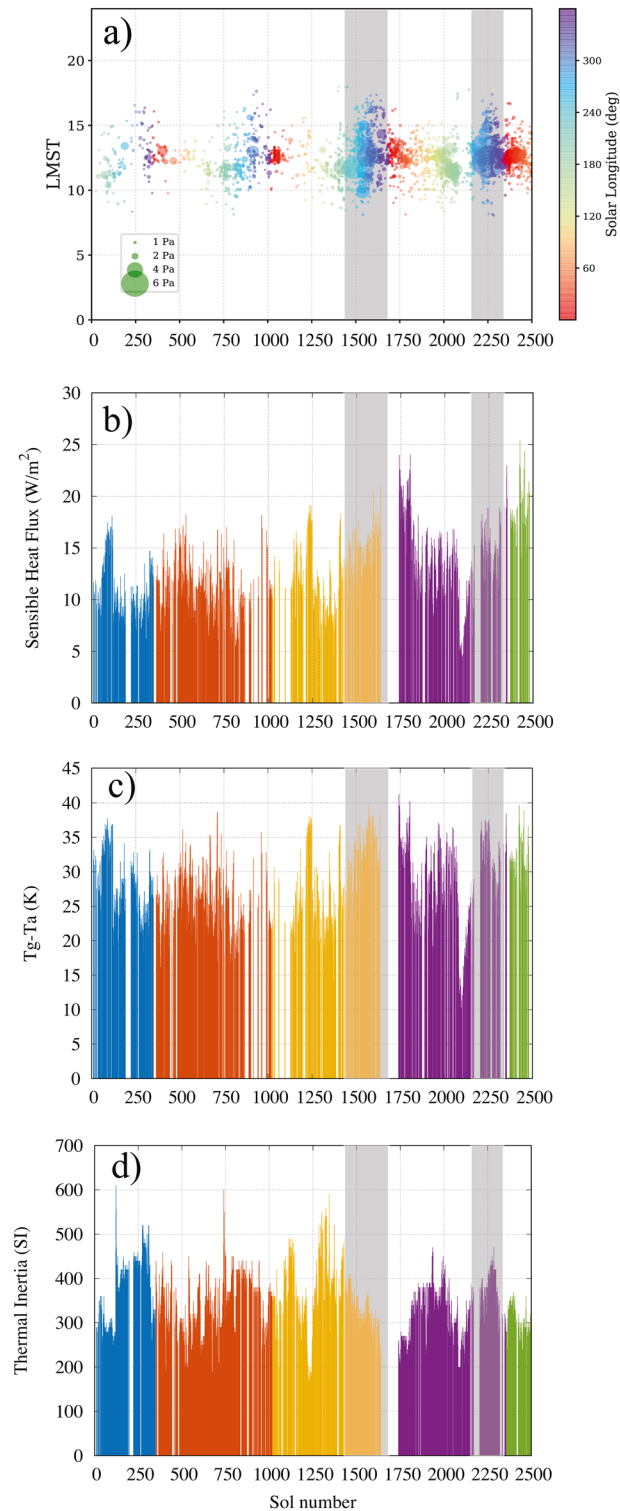
Figure 16. Relation between pressure drops and sensible heat flux as measured by MSL REMS sensors. (a) Daytime pressure drops detected by the REMS instrument as a function of MSL sol (*x*-axis) and LMST (*y*-axis). The size of each bubble corresponds to the intensity of the pressure drop. Solar longitudes are given with a color code as described by the color bar. The shaded area indicates the time periods with the largest number and intensity of convective pressure drops. Data described in Ordóñez-Etxeberria et al. (2020). (b–d) Sol-to-sol evolution of TF, T_g–T_a, and thermal inertia, as a function of sol number, with color code used for MYs 31–35, left to right.

6. Summary and Conclusions

We have used environmental measurements from the REMS and Mastcam instruments to obtain the surface energy budget across Curiosity's traverse during the first 2500 sols (3.7 MYs) of the MSL mission. First-of-their-kind measurements from MSL, in combination with its unprecedented duration and data measuring and storage capabilities, allow for the analyses of the surface energy budget from interannual to diurnal timescales, far exceeding the capabilities of predecessor missions on Mars.

From general to particular, the main conclusions of this article are:

1. Since the latent (<0.1 W/m^2) and sensible (<30 W/m^2) heat fluxes present the lowest values among the SEB terms due to the low water content ($q_a \sim 10^{-4}$) and thin Martian atmosphere ($\rho_a \sim 10^{-2}$ kg m^{-3}), the ground heat flux G virtually accounts for the entire net radiative forcing (R_{NET} = SW↓(1 − α) + LW↓ − LW↑) at Gale. Specifically, the ground heat flux is ∼95% of the net radiative forcing during daytime and around 99% during nighttime, regardless of the season.
2. SW↓ is the primary surface forcing (daily maximum ∼500 W/m^2), presenting a modest seasonal variation (<20%), given the near-equatorial latitude of Gale (4.5°S). LW↓ is typically one order of magnitude lower than the solar forcing, and during the dusty season (Ls = 180°–360°), it shows values twice as large as during the clear season (Ls = 0°–180°). An exception to this occurred during the MY34 global dust storm, when LW↓ became the primary surface forcing.
3. While the interannual evolution of SW↓ and LW↓ is small during the aphelion season (Ls = 0°–180°), it significantly increases during the perihelion season (Ls = 180°–360°) following interannual changes in dust opacity. The most extreme example is the MY 34 global dust storm, when the maximum SW↓ flux was reduced by about 90% and the maximum LW↓ flux was increased by about 100%, as compared to previous years.
4. Changes in dust opacity drive variations in the daily mean LW↓ during the perihelion season, when each relative maximum of opacity coincides with a relative maximum of the daily mean LW↓, provided that there is a temporal overlap between both quantities. During the aphelion season, changes in daily mean near-surface air temperature values, with an annual minimum at Ls ∼ 90°, seem to be more correlated with variations in the daily mean LW↓.
5. The assumption of a homogeneous soil most likely affected our results for G and LW↓ at local times after sunrise and before sunset. This would explain the unexpected "a.m" peak and the "too-large-pm" peak in LW↓ (Figure 9). This is because surfaces with lateral or vertical variations in thermal inertia exhibit distinct phasing at the times of most rapid warming and cooling, coinciding with the periods when observed and SCM-simulated ground temperature present significant departures.
6. The interannual and seasonal variability of the ground heat flux is modest through Ls, and it is primarily caused by changes in thermal inertia.
7. The diurnal variation in sensible heat flux is mainly governed by changes in T_g–T_a, while the seasonal variation is governed by changes in atmospheric density. Moreover, the sol-to-sol variability in the daily maximum TF is strong through its dependence on T_g–T_a, which in turn depends on the sol-to-sol variability in the geophysical properties of the terrain (e.g., thermal inertia) and dust opacity.
8. As open questions left for future study, we plan to assess: (a) the seasonal evolution of surface albedo, based on which values peak between Ls ∼ 210° and 270° every MY, coincident with the peak in aerosol opacity; and (b) the lack of correlation between sensible heat fluxes and pressure drops, based on which increases in vortex activity as measured by REMS cannot be explained only by enhanced TF values (nor by increases in T_g-T_a following a reduction in thermal inertia). This suggests that increases in thermodynamical efficiency (PBL thickening) as the rover ascends Aeolis Mons might play an important role in the development of vortices.

Data Availability Statement

All the values necessary to reproduce each figure shown in this manuscript are archived at the USRA Houston Repository (https://repository.hou.usra.edu/handle/20.500.11753/1766). This repository provides data without restriction or fees.

References

Banfield, D., Spiga, A., Newman, C., Forget, F., Lemmon, M., Lorenz, R., & Lognonné, P. (2020). The atmosphere of Mars as observed by InSight. *Nature Geoscience*, *13*, 190–198. https://doi.org/10.1038/s41561-020-0534-0

Basu, S., Richardson, M. I., & Wilson, R. J. (2004). Simulation of the Martian dust cycle with the GFDL Mars GCM. *Journal of Geophysical Research: Planets*, *109*(E11), E11006. https://doi.org/10.1029/2004je002243

Bell, J. F., III, Rice, M. S., Johnson, J. R., & Hare, T. M. (2008). Surface albedo observations at Gusev crater and Meridiani Planum, Mars. *Journal of Geophysical Research: Planets*, *113*(E6), E06S18. https://doi.org/10.1029/2007je002976

Chen-Chen, H., Perez-Hoyos, S., & Sánchez-Lavega, A. (2020). Dust particle size, shape and optical depth during the 2018/MY34 Martian global dust storm retrieved by MSL Curiosity rover Navigation Cameras. *Icarus*, *354*, 114021.

Christensen, P. R., Wyatt, M. B., Glotch, T. D., Rogers, A. D., Anwar, S., Arvidson, R. E., et al. (2004). Mineralogy at Meridiani Planum from the Mini-TES experiment on the Opportunity Rover. *Science*, *306*(5702), 1733–1739. https://doi.org/10.1126/science.1104909

Davy, R., Davis, J. A., Taylor, P. A., Lange, C. F., Weng, W., Whiteway, J., & Gunnlaugson, H. P. (2010). Initial analysis of air temperature and related data from the Phoenix MET station and their use in estimating turbulent heat fluxes. *Journal of Geophysical Research: Planets*, *115*(E3), E00E13. https://doi.org/10.1029/2009je003444

de la Torre-Juárez, M., Cooper, B., Mischna, M., Lemmon, M. T., Martinez, G., Vasavada, A. R., & Moores, J. E. (2019). Analysis of warm nighttime surface temperature anomalies in gale crater as a potential signature of nighttime clouds. *American Geophysical Union, Fall Meeting*, P41B–3417.

Farley, K. A., Williford, K. H., Stack, K. M., Bhartia, R., Chen, A., de la Torre, M., et al. (2020). Mars 2020 mission overview. *Space Science Reviews*, *216*(8), 1–41. https://doi.org/10.1007/s11214-020-00762-y

Fenton, L. K., Geissler, P. E., & Haberle, R. M. (2007). Global warming and climate forcing by recent albedo changes on Mars. *Nature*, *446*(7136), 646–649. https://doi.org/10.1038/nature05718

Ferri, F., Smith, P. H., Lemmon, M., & Rennó, N. O. (2003). Dust devils as observed by Mars Pathfinder. *Journal of Geophysical Research: Planets*, *108*(E12), 5133. https://doi.org/10.1029/2000je001421

Fischer, E., Martínez, G. M., Rennó, N. O., Tamppari, L. K., & Zent, A. P. (2019). Relative humidity on mars: New results from the phoenix TECP sensor. *Journal of Geophysical Research: Planets*, *124*(11), 2780–2792. https://doi.org/10.1029/2019je006080

Forget, F., Hourdin, F., Fournier, R., Hourdin, C., Talagrand, O., Collins, M., et al. (1999). Improved general circulation models of the Martian atmosphere from the surface to above 80 km. *Journal of Geophysical Research: Planets*, *104*(E10), 24155–24175. https://doi.org/10.1029/1999je001025

Garrat, J. R. (1992). *The atmospheric boundary layer, Cambridge Atmos*. Cambridge Univ. Press.

Gómez-Elvira, J., Armiens, C., Carrasco, I., Genzer, M., Gómez, F., Haberle, R., et al. (2014). Curiosity's rover environmental monitoring station: Overview of the first 100 sols. *Journal of Geophysical Research: Planets*, *119*(7), 1680–1688. https://doi.org/10.1002/2013JE004576

Gómez-Elvira, J., Armiens, C., Castañer, L., Domínguez, M., Genzer, M., Gómez, F., et al. (2012). REMS: The environmental sensor suite for the Mars Science Laboratory rover. *Space Science Reviews*, *170*(1–4), 583–640. https://doi.org/10.1007/978-1-4614-6339-9_17

Gough, R. V., Rapin, W., Martínez, G. M., Meslin, P. Y., Gasnault, O., Schröder, S., & Wiens, R. C. (2020). Possible detection of water frost by the curiosity Rover. *LPI*, *2326*, 2205.

Greybush, S. J., Gillespie, H. E., & Wilson, R. J. (2019). Transient eddies in the TES/MCS ensemble mars atmosphere reanalysis system (EMARS). *Icarus*, *317*, 158–181. https://doi.org/10.1016/j.icarus.2018.07.001

Guzewich, S. D., Lemmon, M., Smith, C. L., Martínez, G., de Vicente-Retortillo, Á., Newman, C. E., et al. (2019). Mars Science Laboratory observations of the 2018/Mars year 34 global dust storm. *Geophysical Research Letters*, *46*(1), 71–79. https://doi.org/10.1029/2018gl080839

Haberle, R. M., McKay, C. P., Pollack, J. B., Gwynne, O. E., Atkinson, D. H., Appelbaum, J., & Flood, D. J. (1993). *Atmospheric effects on the utility of solar power on Mars* (p. 845). Resources of Near-Earth Space.

Hébrard, E., Listowski, C., Coll, P., Marticorena, B., Bergametti, G., Määttänen, A., et al. (2012). An aerodynamic roughness length map derived from extended Martian rock abundance data. *Journal of Geophysical Research: Planets*, *117*(E4). https://doi.org/10.1029/2011je003942

Hong, S. Y., & Pan, H. L. (1996). Nonlocal boundary layer vertical diffusion in a medium-range forecast model. *Monthly Weather Review*, *124*(10), 2322–2339. https://doi.org/10.1175/1520-0493(1996)124<2322:nblvdi>2.0.co;2

Kahanpää, H., Newman, C., Moores, J., Zorzano, M.-P., Martín-Torres, J., Navarro, S., et al. (2016). Convective vortices and dust devils at the MSL landing site: Annual variability. *Journal of Geophysical Research: Planets*, *121*(8), 1514–1549. https://doi.org/10.1002/2016JE005027

Kahre, M. A., Murphy, J. R., & Haberle, R. M. (2006). Modeling the Martian dust cycle and surface dust reservoirs with the NASA Ames general circulation model. *Journal of Geophysical Research: Planets*, *111*(E6), E06008. https://doi.org/10.1029/2005je002588

Lemmon, M. T., Guzewich, S. D., McConnochie, T., de Vicente-Retortillo, A., Martínez, G., Smith, M. D., et al. (2019). Large dust aerosol sizes seen during the 2018 Martian global dust event by the Curiosity rover. *Geophysical Research Letters*, *46*(16), 9448–9456. https://doi.org/10.1029/2019gl084407

Lorenz, R. D., Lemmon, M. T., Maki, J., Banfield, D., Spiga, A., Charalambous, C., & Banerdt, W. B. (2020). Scientific observations with the insight solar arrays: Dust, clouds, and eclipses on Mars. *Earth and Space Science*, *7*(5), e2019EA000992. https://doi.org/10.1029/2019ea000992

Määttänen, A., & Savijärvi, H. (2004). Sensitivity tests with a one-dimensional boundary-layer Mars model. *Boundary-Layer Meteorology*, *113*(3), 305–320. https://doi.org/10.1007/s10546-004-5274-y

Madeleine, J. B., Forget, F., Millour, E., Montabone, L., & Wolff, M. J. (2011). Revisiting the radiative impact of dust on Mars using the LMD Global Climate Model. *Journal of Geophysical Research: Planets*, *116*(E11), E1101. https://doi.org/10.1029/2011je003855

Martínez, G. M., Newman, C. N., De Vicente-Retortillo, A., Fischer, E., Renno, N. O., Richardson, M. I., et al. (2017). The modern near-surface martian climate: A review of in-situ meteorological data from Viking to Curiosity. *Space Science Reviews*, *212*(1–2), 295–338. https://doi.org/10.1007/s11214-017-0360-x

Martínez, G. M., Fischer, E., Rennó, N. O., Sebastián, E., Kemppinen, O., Bridges, N., et al. (2016). Likely frost events at Gale crater: Analysis from MSL/REMS measurements. *Icarus*, *280*, 93–102. https://doi.org/10.1016/j.icarus.2015.12.004

Martínez, G. M., Rennó, N., Fischer, E., Borlina, C. S., Hallet, B., De La Torre Juárez, M., et al. (2014). Surface energy budget and thermal inertia at Gale Crater: Calculations from ground-based measurements. *Journal of Geophysical Research: Planets*, *119*(8), 1822–1838. https://doi.org/10.1002/2014je004618

Möhlmann, D. T. (2004). Water in the upper martian surface at mid-and low-latitudes: Presence, state, and consequences. *Icarus*, *168*(2), 318–323. https://doi.org/10.1016/j.icarus.2003.11.008

Newman, C. E., Gómez-Elvira, J., Marin, M., Navarro, S., Torres, J., Richardson, M. I., et al. (2017). Winds measured by the Rover Environmental Monitoring Station (REMS) during the Mars Science Laboratory (MSL) rover's Bagnold Dunes Campaign and comparison with numerical modeling using MarsWRF. *Icarus*, *291*, 203–231. https://doi.org/10.1016/j.icarus.2016.12.016

Newman, C. E., Kahanpää, H., Richardson, M. I., Martínez, G. M., Vicente-Retortillo, Á., & Lemmon, M. T. (2019). Mars WRF Convective Vortex and Dust Devil Predictions for Gale Crater Over 3 Mars Years and Comparison With MSL-REMS Observations. *Journal of Geophysical Research: Planets*, *124*(12), 3442–3468. https://doi.org/10.1029/2019je006082

Ordóñez-Etxeberria, I., Hueso, R., & Sánchez-Lavega, A. (2018). A systematic search of sudden pressure drops on Gale crater during two Martian years derived from MSL/REMS data. *Icarus*, *299*, 308–330. https://doi.org/10.1016/j.icarus.2017.07.032

Ordóñez-Etxeberria, I., Hueso, R., & Sánchez-Lavega, A. (2020). Strong increase in dust devil activity at Gale crater on the third year of the MSL mission and suppression during the 2018 Global Dust Storm. *Icarus*, *347*, 113814. https://doi.org/10.1016/j.icarus.2020.113814

Pla-Garcia, J., Rafkin, S. C., Kahre, M., Gomez-Elvira, J., Hamilton, V. E., Navarro, S., et al. (2016). The meteorology of Gale crater as determined from rover environmental monitoring station observations and numerical modeling. Part I: Comparison of model simulations with observations. *Icarus*, *280*, 103–113. https://doi.org/10.1016/j.icarus.2016.03.013

Rafkin, S. C. R., Haberle, R. M., & Michaels, T. I. (2001). The Mars Regional Atmospheric Modeling System (MRAMS): Model description and selected simulations. *Icarus*, *151*, 228–256. https://doi.org/10.1006/icar.2001.6605

Rennó, N. O., Burkett, M. L., & Larkin, M. P. (1998). A simple thermodynamic theory for dust devils. *Journal of the Atmospheric Sciences*, *55*, 3244–3252. https://doi.org/10.1175/1520-0469(1998)055<3244:asttfd>2.0.co;2

Rivera-Valentín, E. G., Chevrier, V. F., Soto, A., & Martínez, G. (2020). Distribution and habitability of (meta) stable brines on present-day Mars. *Nature Astronomy*, *4*, 1–6. https://doi.org/10.1038/s41550-020-1080-9

Rivera-Valentín, E. G., Gough, R. V., Chevrier, V. F., Primm, K. M., Martínez, G. M., & Tolbert, M. (2018). Constraining the potential liquid water environment at Gale crater, Mars. *Journal of Geophysical Research: Planets*, *123*(5), 1156–1167. https://doi.org/10.1002/2018JE005558

Rodriguez-Manfredi, J. A., Alonso, A., Apestigue, V., Arruego, I., Banfield, D., Boland, J., et al. (2020). The Mars environmental dynamics analyzer. A suite of sensors for the Mars 2020 mission. *Space Science Reviews*, *217*(3), 1–86.

Sánchez-Lavega, A., del Río-Gaztelurrutia, T., Hernández-Bernal, J., & Delcroix, M. (2019). The onset and growth of the 2018 Martian global dust storm. *Geophysical Research Letters*, *46*(11), 6101–6108.

Savijärvi, H. (1995). Mars boundary layer modeling: Diurnal moisture cycle and soil properties at the Viking Lander 1 site. *Icarus*, *117*(1), 120–127. https://doi.org/10.1006/icar.1995.1146

Savijärvi, H. (1999). A model study of the atmospheric boundary layer in the Mars Pathfinder lander conditions. *Quarterly Journal of the Royal Meteorological Society*, *125*(554), 483–493. https://doi.org/10.1002/qj.49712555406

Savijärvi, H. (2012). The convective boundary layer on Mars: Some 1-D simulation results. *Icarus*, *221*(2), 617–623. https://doi.org/10.1016/j.icarus.2012.08.016

Savijärvi, H. (2014). A toy climate model for Mars. *Icarus*, *242*, 105–111. https://doi.org/10.1016/j.icarus.2014.07.029

Savijärvi, H., Crisp, D., & Harri, A. M. (2005). Effects of CO_2 and dust on present-day solar radiation and climate on Mars. *Quarterly Journal of the Royal Meteorological Society*, *131*(611), 2907–2922. https://doi.org/10.1256/qj.04.09

Savijärvi, H., Harri, A. M., & Kemppinen, O. (2016). The diurnal water cycle at Curiosity: Role of exchange with the regolith. *Icarus*, *265*, 63–69. https://doi.org/10.1016/j.icarus.2015.10.008

Savijärvi, H., & Kauhanen, J. (2008). Surface and boundary-layer modelling for the Mars Exploration Rover sites. *Quarterly Journal of the Royal Meteorological Society: A journal of the atmospheric sciences, applied meteorology and physical oceanography*, *134*(632), 635–641. https://doi.org/10.1002/qj.232

Savijärvi, H., & Määttänen, A. (2010). Boundary-layer simulations for the Mars Phoenix lander site. *Quarterly Journal of the Royal Meteorological Society*, *136*(651), 1497–1505. https://doi.org/10.1002/qj.650

Savijärvi, H., Martinez, G., Harri, A. M., & Paton, M. (2020). Curiosity observations and column model integrations for a martian global dust event. *Icarus*, *337*, 113515. https://doi.org/10.1016/j.icarus.2019.113515

Savijärvi, H., McConnochie, T. H., Harri, A. M., & Paton, M. (2019). Water vapor mixing ratios and air temperatures for three martian years from Curiosity. *Icarus*, *326*, 170–175. https://doi.org/10.1016/j.icarus.2019.03.020

Savijärvi, H., Paton, M., & Harri, A. M. (2018). New column simulations for the Viking landers: Winds, fog, frost, adsorption? *Icarus*, *310*, 48–53. https://doi.org/10.1016/j.icarus.2017.11.007

Sebastián, E., Martínez, G., Ramos, M., Haenschke, F., Ferrándiz, R., Fernández, M., & Manfredi, J. A. R. (2020). Radiometric and angular calibration tests for the MEDA-TIRS radiometer onboard NASA's Mars 2020 mission. *Measurement*, *164*, 107968. https://doi.org/10.1016/j.measurement.2020.107968

Smith, M. D., Bandfield, J. L., & Christensen, P. R. (2000). Separation of atmospheric and surface spectral features in Mars Global Surveyor Thermal Emission Spectrometer (TES) spectra. *Journal of Geophysical Research: Planets*, *105*(E4), 9589–9607. https://doi.org/10.1029/1999je001105

Smith, M. D., Conrath, B. J., Pearl, J. C., & Ustinov, E. A. (1996). Retrieval of atmospheric temperatures in the Martian planetary boundary layer using upward-looking infrared spectra. *Icarus*, *124*(2), 586–597. https://doi.org/10.1006/icar.1996.0232

Smith, M. D., Wolff, M. J., Lemmon, M. T., Spanovich, N., Banfield, D., Budney, C. J., et al. (2004). First atmospheric science results from the Mars Exploration Rovers Mini-TES. *Science*, *306*(5702), 1750–1753. https://doi.org/10.1126/science.1104257

Smith, M. D., Wolff, M. J., Spanovich, N., Ghosh, A., Banfield, D., Christensen, P. R., & Squyres, S. W. (2006). One Martian year of atmospheric observations using MER Mini-TES. *Journal of Geophysical Research: Planets*, *111*(E12), E12S13. https://doi.org/10.1029/2006je002770

Smith, M. D., Zorzano, M. P., Lemmon, M., Martin-Torres, J., & de Cal, T. M. (2016). Aerosol optical depth as observed by the Mars Science Laboratory REMS UV photodiodes. *Icarus*, *280*, 234–248. https://doi.org/10.1016/j.icarus.2016.07.012

Smith, P. H., Tamppari, L. K., Arvidson, R. E., Bass, D., Blaney, D., Boynton, W. V., et al. (2009). H_2O at the Phoenix landing site. *Science*, *325*(5936), 58–61. https://doi.org/10.1126/science.1172339

Spanovich, N., Smith, M. D., Smith, P. H., Wolff, M. J., Christensen, P. R., & Squyres, S. W. (2006). Surface and near-surface atmospheric temperatures for the Mars Exploration Rover landing sites. *Icarus*, *180*(2), 314–320. https://doi.org/10.1016/j.icarus.2005.09.014

Spiga, A., Forget, F., Lewis, S. R., & Hinson, D. P. (2010). Structure and dynamics of the convective boundary layer on Mars as inferred from large-eddy simulations and remote-sensing measurements. *Quarterly Journal of the Royal Meteorological Society: A journal of the atmospheric sciences, applied meteorology and physical oceanography*, *136*(647), 414–428. https://doi.org/10.1002/qj.563

Spiga, A., Murdoch, N., Lorenz, R., Forget, F., Newman, C., Rodriguez, S., et al. (2020). *A study of daytime convective vortices and turbulence in the martian Planetary Boundary Layer based on half-a-year of InSight atmospheric measurements and Large-Eddy Simulations*. arXiv preprint arXiv:2005.01134.

Steakley, K., & Murphy, J. (2016). A year of convective vortex activity at Gale crater. *Icarus*, *278*, 180–193. https://doi.org/10.1016/j.icarus.2016.06.010

Stensrud, D. J. (2009). *Parameterization schemes: Keys to understanding numerical weather prediction models*. Cambridge University Press.

Stull, R. B. (2012). An Introduction to Boundary Layer Meteorology (Vol. 13). Springer Science & Business Media.

Sutton, J. L., Leovy, C. B., & Tillman, J. E. (1978). Diurnal variations of the Martian surface layer meteorological parameters during the first 45 sols at two Viking lander sites. *Journal of the Atmospheric Sciences*, *35*(12), 2346–2355. https://doi.org/10.1175/1520-0469(1978)035<2346:dvotms>2.0.co;2

Szwast, M. A., Richardson, M. I., & Vasavada, A. R. (2006). Surface dust redistribution on Mars as observed by the Mars Global Surveyor and Viking orbiters. *Journal of Geophysical Research: Planets*, *111*(E11), E11008. https://doi.org/10.1029/2005je002485

Tabataba-Vakili, F., Read, P. L., Lewis, S. R., Montabone, L., Ruan, T., Wang, Y., & Young, R. M. (2015). A Lorenz/Boer energy budget for the atmosphere of Mars from a "reanalysis" of spacecraft observations. *Geophysical Research Letters*, *42*(20), 8320–8327.

Tillman, J. E., Landberg, L., & Larsen, S. E. (1994). The boundary layer of Mars: Fluxes, stability, turbulent spectra, and growth of the mixed layer. *Journal of the Atmospheric Sciences*, *51*(12), 1709–1727. https://doi.org/10.1175/1520-0469(1994)051<1709:tblomf>2.0.co;2

Vaniman, D. T., Martínez, G. M., Rampe, E. B., Bristow, T. F., Blake, D. F., Yen, A. S., et al. (2018). Gypsum, bassanite, and anhydrite at Gale crater, Mars. *American Mineralogist*, *103*(7), 1011–1020. https://doi.org/10.2138/am-2018-6346

Vasavada, A. R., Piqueux, S., Lewis, K. W., Lemmon, M. T., & Smith, M. D. (2017). Thermophysical properties along Curiosity's traverse in Gale crater, Mars, derived from the REMS ground temperature sensor. *Icarus*, *284*, 372–386. https://doi.org/10.1016/j.icarus.2016.11.035

Vicente-Retortillo, A., Martínez, G. M., Lemmon, M. T., Renno, N. O., & Rodríguez-Manfredi, J. A. (2021). Diurnal variations in atmospheric opacity at Gale Crater, Mars. In Lunar and Planetary Science Conference (Vol. 2548, p. 1419).

Vicente-Retortillo, Á., Martínez, G. M., Renno, N., Newman, C. E., Ordóñez-Etxeberria, I., Lemmon, M. T., & Sánchez-Lavega, A. (2018). Seasonal deposition and lifting of dust on Mars as observed by the Curiosity rover. *Scientific Reports*, *8*(1), 1–8. https://doi.org/10.1038/s41598-018-35946-8

Vicente-Retortillo, Á., Martínez, G. M., Renno, N. O., Lemmon, M. T., & de la Torre-Juárez, M. (2017). Determination of dust aerosol particle size at Gale Crater using REMS UVS and Mastcam measurements. *Geophysical Research Letters*, *44*(8), 3502–3508.

Vicente-Retortillo, A., Martínez, G. M., Rennó, N. O., Lemmon, M. T., de la Torre-Juárez, M., & Gómez-Elvira, J. (2020). In Situ UV measurements by MSL/REMS: Dust deposition and angular response corrections. *Space Science Reviews*, *216*(5), 1–19. https://doi.org/10.1007/s11214-020-00722-6

Vicente-Retortillo, Á., Valero, F., Vázquez, L., & Martínez, G. M. (2015). A model to calculate solar radiation fluxes on the Martian surface. *Journal of Space Weather and Space Climate*, *5*, A33. https://doi.org/10.1051/swsc/2015035

Viúdez-Moreiras, D., Gómez-Elvira, J., Newman, C. E., Navarro, S., Marin, M., Torres, J., & de la Torre-Juárez, M. (2019). Gale surface wind characterization based on the Mars Science Laboratory REMS dataset. Part I: Wind retrieval and Gale's wind speeds and directions. *Icarus*, *319*, 909–925. https://doi.org/10.1016/j.icarus.2018.10.011

Viúdez-Moreiras, D., Gómez-Elvira, J., Newman, C. E., Navarro, S., Marin, M., Torres, J., & de la Torre-Juárez, M. (2019). Gale surface wind characterization based on the Mars Science Laboratory REMS dataset. Part II: Wind probability distributions. *Icarus*, *319*, 645–656. https://doi.org/10.1016/j.icarus.2018.10.010

Wolff, M. J., Clancy, R. T., Goguen, J. D., Malin, M. C., & Cantor, B. A. (2010). Ultraviolet dust aerosol properties as observed by MARCI. *Icarus*, *208*(1), 143–155. https://doi.org/10.1016/j.icarus.2010.01.010

Wolff, M. J., Smith, M. D., Clancy, R. T., Arvidson, R., Kahre, M., Seelos, F., & Savijärvi, H. (2009). Wavelength dependence of dust aerosol single scattering albedo as observed by the Compact Reconnaissance Imaging Spectrometer. *Journal of Geophysical Research: Planets*, *114*(E2). https://doi.org/10.1029/2009je003350

Wu, Z., Richardson, M. I., Zhang, X., Cui, J., Heavens, N. G., Lee, C., et al. (2021). Large Eddy Simulations of the Dusty Martian Convective Boundary Layer with Mars WRF. *Journal of Geophysical Research: Planets*, *126*. e2020JE006752, https://doi.org/10.1029/2020JE006752

Zent, A. P., Hecht, M. H., Cobos, D. R., Wood, S. E., Hudson, T. L., Milkovich, S. M., & Mellon, M. T. (2010). Initial results from the thermal and electrical conductivity probe (TECP) on Phoenix. *Journal of Geophysical Research: Planets*, *115*(E3), E00E14. https://doi.org/10.1029/2009je003420